Surficial permeability of the axial valley seafloor; Endeavour Segment, Juan de Fuca Ridge

Casey K. Hearn
School of Oceanography, University of Washington,
Seattle, Washington 98195-7940, USA
(ckh3@u.washington.edu)

Kira L. Homola
School of Oceanography, University of Washington,
Seattle, Washington 98195-7940, USA
(khomola@u.washington.edu)

H. Paul Johnson
School of Oceanography, University of Washington,
Seattle, Washington 98195-7940, USA
(johnson@ocean.washington.edu)

University of Washington
Department of Oceanography
Washington, USA

Key Points

- Permeability of the seafloor surface veneer is a boundary condition for circulation models
- Sea floor permeability is non-uniform through the axial valley at Juan de Fuca Ridge
- Hydrothermal systems may respond to temporal changes in surface permeability

Keywords: hydrothermal circulation, Juan de Fuca Ridge, seafloor permeability, Endeavour

Abstract

[1] Hydrothermal systems at mid-ocean spreading centers play a fundamental role in Earth's geothermal budget. One under-examined facet of marine hydrothermal systems is the role that permeability of the uppermost seafloor veneer plays in the distribution of hydrothermal fluid. As both the initial and final vertical gateway for sub-surface fluid circulation, uppermost seafloor permeability may influence the local spatial distribution of hydrothermal flow. A method of deriving a photomosaic from seafloor video was developed and utilized to estimate relative surface permeability in an active hydrothermal area on the Endeavour Segment of the Juan de Fuca Ridge. The resulting mosaic of seafloor geology provided sub-meter resolution of the axial valley seafloor over an area exceeding 1 km^2. Results indicate that the valley walls and basal talus slope are topographically rugged and unsedimented, providing minimal resistance to fluid transmission. The axial valley floor is capped by an unbroken blanket of low permeability sediment, resisting fluid exchange with the subsurface reservoir. Active fluid emission sites were restricted to the high-permeability zone at the base of the western wall. A series of inactive fossil hydrothermal structures form a linear trend along the western bounding wall, oriented orthogonal to the spreading axis. High temperature vent locations appear to have migrated over 100 meters along-ridge-strike over the decade between surveys. This spatial pattern suggests an evolutionary sequence for hydrothermal fields where changes in seafloor permeability may be a secondary contributing factor in the migration of emission sites, both along-strike and in the cross axis direction.

1. Introduction

1.1 General Information

[2] The surface veneer of volcanic rock outcrops and sediment cover at the seafloor represents a critical gateway for fluids both entering and exiting the subsurface hydrothermal reservoir at mid-ocean ridges. Although the uppermost few hundreds of meters of igneous crust at the Juan de Fuca spreading center has a high porosity and presumably a high permeability (Gilbert & Johnson, 1999), previous, non-systematic observations of the axial valley seafloor at Endeavour indicate the presence of large areas with unbroken basalt flows or nearly complete sediment cover that would limit the transmission of fluid either into or out of the sub-surface. This study attempts to interpret relative seafloor permeability from a systematic seafloor imaging survey of a portion of the axial valley surface geology. Surface permeability throughout the axial valley floor is an important but largely unevaluated boundary condition for modeling fluid circulation of the axial hydrothermal systems at the Endeavour segment and at other spreading centers.

[3] Hydrothermal fluid circulation through oceanic crust is estimated to provide ~25% of the Earth's surface heat flux [*Stein and Stein*, 1994]. Understanding marine hydrothermal circulation is required to constrain the planetary heat budget and to define a system that provides energy and nutrients to chemosynthetic communities, Earth's oldest surviving ecosystem [*Childress and Fisher*, 1995]. Among the remaining principal undefined parameters for hydrothermal systems are the circulation pathways, depth of penetration, velocities, and residence times of fluid traveling through the subsurface. Seafloor hydrothermal systems vary widely on a global scale, and models of fluid circulation for a given system must necessarily be based on local conditions.

[4] There are currently three generalized models proposed to describe the circulation pathways of fluid in hydrothermal systems at medium-to- fast-spreading mid-ocean ridges: (1) seawater enters the subsurface along deep, normal faults at one or both edges of the axial valley, then flows across-axis to emerge as high temperature outflow in the center of the valley or on the side opposite the recharge zone [*Williams et al*., 1979; *Johnson et al.* 2010], (2) fluid circulation takes place primarily within individual faults that are oriented along-strike and parallel to the ridge axis in distinct slot convection cells [*Rabinowicz et al*., 1999; *Wilcock*, 1998; *Tolstoy et al*., 2008], (3) fluid convects in a basement layer with uniformly isotropic permeability as annular rings with broad circular recharge areas surrounding narrow up-flow regions [*Coumou et al*., 2008; *Tivey and Johnson*, 2002: *Johnson et al*., 2010]. Each of these models appears to be applicable for specific hydrothermal vent systems located on spreading centers within a different geological environment. While these models have utilized a wide range of data types and boundary conditions, the potential for the possible influence of the permeability of the surficial seafloor has not been considered, due largely to the lack of appropriate data.

[5] A novel method for estimating seafloor surface permeability is the use of meter-scale high-resolution photomosaics constructed from video footage taken during Remotely Operated Vehicle (ROV) transects over a large area of the seafloor. Although multibeam swath bathymetry and side-scan sonar data are useful for identifying features on a scale of tens to hundreds of meters, visual observations from submersibles and photomosaics from remote cameras are required for accurately identifying the location and lateral extent of hydrothermal and volcanic features on the scale of 10^{-1} to 10^{+2} meters [*Robigou et al*., 1993; *Escartin et al*., 2008]. As

examples, *Lessard-Pilon et al*. [2010] used photomosaic images of cold seep communities in the Gulf of Mexico to describe changes in environmental conditions over small spatial and temporal scales and described how the composition of associated biological communities responded to these changes. *Mittelstaedt et al*. [2012] quantified the heat flux from diffuse and discrete venting using photomosaics and video velocity analysis of outflow at the Lucky Strike hydrothermal field on the Mid-Atlantic ridge. Temporal changes in heat flux in this study were quantified using analysis of the spatial extent of bacterial mats and proximity to faults. The Lucky Strike study utilized specialized software to create extensive photomosaics of the seafloor with a precision sufficient for accurate comparison of images obtained separated by several years [*Barreyre and Escartín et al*., 2012]. The present project utilizes photomosaic interpretive techniques to study the seafloor of the RAVEN portion of the Endeavour segment of the Juan de Fuca spreading ridge (Figure 1).

1.2 Endeavour Background

[6] The axial magma lens beneath the Endeavour Segment has been imaged seismically as a mid-crustal reflector 2.1 to 2.4 km below the seafloor that underlies all of the known hydrothermal vent fields [*Van Ark et al*., 2007; *Wilcock et al*., 2009; *Kelley et al*., 2012]. The zone of partial melt beneath the Endeavour Segment extends approximately 24 km along-axis and 0.4 to 1.2 km across-axis, with the non-horizontal upper surface dipping to the east with slopes that vary from 8° to 36° [*Van Ark et al*., 2007]. Episodic replenishment of partial melt occurs along the Endeavour magma lens, providing the periodically renewed heat source previously suggested as a requirement for long-lived, extensive hydrothermal circulation systems [*Wilcock et al*., 2009].

[7] Seismic velocities for the axial portion of Layer 2A at the Endeavour Segment are exceptionally low, in some areas approaching1.8 km/s [*Van Ark et al*., 2007], suggesting a very high porosity of up to 30% for the uppermost 350 m of basalt [*Nedimović* et al., 2008]. The immediately underlying 2B layer on axis has an average seismic velocity near 5.2 km/s [*Newman et al*., 2011]. Upper crustal densities based on seafloor gravity measurements at the axis are also quite low, supporting a high subsurface porosity of >30% for the uppermost crust at the Juan de Fuca Ridge [*Holmes and Johnson*, 1993; *Gilbert and Johnson*, 1999]. For fluid flow estimates, we used the established correlation between seismic velocity and permeability for upper crust from *Carlson* [2011]

$$log(\kappa) = -(7.4 \pm 0.7) - (1.3 \pm 0.1)v \quad (1)$$

along with average measured seismic velocities of 2.5 km/s in Layer 2A at Endeavour from *Nedimović* et al. [2008] to estimate uppermost crustal permeability ranging from 2×10^{-9} to 2.5×10^{-11} m^2. Similarly estimated permeability for the underlying Layer 2B was lower on axis at ~1.6×10^{-14} m^2 using seismic velocity from *Newman* et al. [2011]. The resulting general model for circulation includes a highly permeable upper layer overlying a relatively low permeability layer of dikes or altered transition zone material. In contrast to the upper crustal layers of extrusive lavas, the composite hemipelagic sediment and fine-grained turbidites common to the Juan de Fuca Ridge flank have a significantly lower permeability, ranging from 10^{-15} to 10^{-18} m^2 [*Giambalvo et al*., 2000]. Comparatively, at the Mid-Atlantic ridge flank, *in situ* sediment permeability at shallow burial depths (<3 m) was measured at 7.55×10^{-16} [*Langseth et al*. 1992]. Due to the small thermal buoyancy forces driving fluid circulation on the ridge flanks, and the low permeability of sediments on the ridge flanks, only minimal fluid seepage has been reported for sediment layers less than tens of meters thick [*Giambalvo et al*. 2000; *Spinelli et al*. 2004; *Hutnak et al*. 2006].

[8] Additional constraints for hydrothermal fluid circulation pathways at the axis of the Endeavour segment were proposed by *Johnson et al*. [2010] using a series of bare-rock conductive heat flow measurements across the axial valley. This heat flow data suggested that multiple circulation modes may exist simultaneously at the nearby Main Endeavour Field. This previous model, based on the distribution of conductive heat flow, proposed a dual nested system of fluid circulation pathways. The high temperature vents were supplied by a deeply circulating pathway that extended from the initial seawater recharge sites at the base of the eastern valley wall to the high temperature discharge sites at the base of the western wall. The secondary system is located in shallow crust above the deep high temperature circulation system, and that seawater recharge zone is located within only a few tens of meters from the low temperature diffuse outflow zones that surround the high temperature emission sites [*Lowell et al*., 2012]. In the interest of improving hydrothermal circulation models at mid-ocean ridge systems, additional parameters for the control of fluid flow should be considered. The purpose of this paper is to investigate the effect of the incomplete sedimentation of a portion of the axial valley in the Endeavour Segment of the Juan de Fuca ridge.

2. Methods

2.1 Project Goals

[9] The goal of this project was to generate a map of the surface geology of a portion of the Endeavour axial valley with compiled photomosaic images using inexpensive commercially available software, and then to interpret it in terms of the relative permeability of the seafloor. The photographic data were collected from two ROV *JASON II* dives on the RAVEN hydrothermal field (see supplemental materials, Figure B). The southern boundary of this area is located ~100 meters north-east along axis from the northern boundary of the well-studied Main Endeavour Hydrothermal Field [*Johnson et al*., 2010; *Kelley et al*., 2012] (Figure 1). These dives were conducted primarily for research goals other than video imaging, including the acquisition of bare-rock conductive heat flow, crustal magnetization, and bottom water temperature data [*Salmi et al*., 2012]. The video images were acquired continuously during the dives, standard geometric transformations were applied, and ArcGIS tool functions were used to obtain images that were aligned, warped, and spatially co-registered to create a photomosaic of a 0.8 by 1.0 km area of the axial valley, largely centered on the small RAVEN hydrothermal field. Bottom water temperature data from a ROV hull-mounted CTD (conductivity, temperature, depth) were acquired simultaneously and used to identify sites of active fluid emission within the study area. These data were compiled into a high resolution map of seafloor geology and near-bottom water temperatures that were interpreted in terms of the permeability of the uppermost surface of the crustal reservoir, in order to constrain circulation models of a small and isolated axial valley hydrothermal system.

[10] The project intended to identify spatial patterns in upper seafloor surface permeability within the Endeavour axial valley at the RAVEN vent field through semi-quantitative analysis of ROV video images. However, the surface relative permeability, which is inferred from seafloor

geological classification and degree of sediment cover, is clearly not representative of the sub-surface crust of Layer 2A. Geological features which are visible at the surface may not extend to depth below the surface; an example being high permeability talus piles which could overlie intact basaltic sheet flows of low permeability. Nevertheless, fluid that either enters or leaves the sub-surface fluid reservoir must pass through the observable seafloor veneer. Thus, while our study provides no information directly relating to fluid flow within the subsurface crustal reservoir, estimates of surface permeability provide useful localized boundary conditions on the sites of potential inflow and outflow, since fluid either entering or leaving the sub-surface must pass through this veneer.

2.2 Data Acquisition

[11] Raw image sets were derived from the video recording system mounted on the ROV *JASON II*, and acquired in 2011 during dives 586 and 590. The *JASON II* navigation system utilizes an ultra-short baseline transponder (USBL). Absolute navigation errors after post-processing are conservatively estimated at less than 10 meters, although our ability to easily re-locate instruments, even at sites with poor visibility, suggests a precision roughly a factor of two better than this. Comparison of cross-track image feature alignment also suggests both the accuracy and precision errors may be closer to 1-2 meters. Standard resolution (non-HD) video recordings were maintained for three on-board cameras throughout all ROV dives on the cruise, providing multiple simultaneous viewpoints. For the purposes of constructing the primary photographic mosaic, the video camera on the brow of the vehicle was used exclusively for the following reasons: (1) the camera position provided the most uniformly continuous coverage of the seafloor, (2) obstructions to the field of view were minimal (3) the camera orientation relative to

the vehicle and zoom settings were held constant throughout all dives, allowing a standardized image transformation method to be used for all obtained images. The camera equipped for these dives was an *Insite Pacific* MINI ZEUS high definition color camera with an 85° horizontal by 64° vertical viewing angle when held at the lowest zoom setting, with a 5.1 mm lens diameter. The brow camera was located above the center of the leading edge of the vehicle (see supplemental materials, Figure A). The camera's point of view was 36.5 cm forward, 227.3 cm above, and directly in line with the vehicle's navigational nodal point along the long axis. All navigation data points were adjusted for this discrepancy. The ROV was tasked entirely with instrument deployment and recovery during the dives and did not perform a regular survey pattern. The altitude was not held constant during transit, although an effort was made to keep seafloor features in view for logging purposes.

2.3 Image registration and preparation

[12] Video files were processed using Freestudio's "Video to JPG Converter" to extract approximately 300,000 frame-grab images from the continuous video at 3-second intervals. The oblique camera angle and position required all images to be cropped at consistent pixel distances from the frame edges. This editing removed areas of the images that were poorly illuminated or obscured by the vehicle frame or static instrument positions. Movable structures, including manipulator arms and the extendable equipment basket, occasionally entered the frame and required additional manual processing to maintain quality. Although camera orientation was fixed, the ROV lighting system configuration changed depending on dive objectives, altering seafloor illumination from dive to dive. However, these changes were not logged and an image lighting correction was not attempted.

2.4 Image Selection

[13] An automated image selection process was designed to provide optimal seafloor area coverage while reducing the distortion and blurring caused by minor misalignment of multiple images in areas of high image density. To reduce image clustering, a minimal horizontal separation of 3 meters in vehicle position was required for consecutive images. Images were sampled frequently when vehicle transit speeds over the bottom approached the maximum of 0.5 meter/second, and sampled less often when the vehicle progress was slow or stopped. An altitude filter of 12.2 meters was used to remove images where the lighting and visibility were inadequate for feature recognition. Over areas of smooth terrain, this filtering process resulted in optimal photographic coverage and feature clarity. In contrast, regions of rough topography or extremely varied terrain produced image clustering or gaps in the mosaic.

2.5 Altimeter

[14] The ROV was equipped with fiber optic north-seeking gyro, solid state flux-gate compass, and 300 kHz Benthos altimeter with a 30 meter range. The altimeter had a low signal-to-noise ratio, and was particularly noisy over rough terrain. Given the need for high quality navigation and attitude information for accurate image projection and alignment, substantial smoothing of the altimeter data was required. A 13-second moving average was used to reduce misalignment between consecutive images, and was forward-stepped to remove artificial lag times.

2.6 Image Projection

[15] An algorithm was constructed to convert raw navigation data and camera configuration into accurate image position, orientation, and scaling within a two-dimensional geospatial framework (see supplemental materials, Figure A). This process utilized trigonometric transformations to account for variations in vehicle position, heading, altitude, pitch, and roll. The algorithm calculated the coordinate points for the four corners of the projected image using an idealized flat projection surface. This spatial data was merged with sub-sampled images to supply the GIS software with all requisite parameters for mosaic production. Within the ArcGIS Data Management toolbox, the 'Warp' function was used to transform images which had been photographed at oblique angles into horizontally projected and geo-referenced two-dimensional representations of the seafloor (Figure 2).

2.7 Mosaic Construction

[16] After projection onto a horizontal plane, all images were subjected to final manual filtering to remove images based on the following criteria: (1) images showing portions of vehicle or attached equipment, (2) images containing a large amount of disturbed sediment in the water column that obscured the seafloor, (3) images where illumination, contrast, or distance prevented recognition of geological features on the seafloor. Once selected for quality, the individual images were merged into a dataset as a continuous one-dimensional track-line image within ArcGIS. A distance-weighted blend function was chosen to reduce contrasting edges between overlapping images. Since physical dimensions and resolution for a fixed image are inherently inversely proportional, smaller images were given priority in any overlap with larger images.

2.8 Creation of geologic map

[17] A manual interpretive method was used in the creation of geologic maps from the linear image mosaics. Each individual track-line mosaic was analyzed independently to improve consistency and reduce regional bias. Classification of seafloor features utilized an along-track approach designed to identify small selections of the seafloor with homogenous features. Polygonal shapes representing specific geological classes were drawn over each feature in the track-line image, and all borders between polygons were artificially forced to be contiguous and without overlap (Figure 2). Viewing scale of the mosaic was maintained uniformly throughout the process at 1:100. Classification of features fell into 5 main geological categories (Figure 3), with separate designations for rare or specialized features. The classification scheme was based on the following criteria: (1) Unbroken Sediment: uniform covering of 100% sediment, underlying geologic features not visible or not identifiable, no outcroppings, no cracks, (2) Sedimented Flows: light to thick sediment draping over recognizable flow or talus morphology, occasional basalt outcroppings, small cracks, (3) Broken Flows: sediment-free or only light sediment draping, loosely assorted material of varying shapes and sizes, numerous small voids and small gaps between basalt rocks, (4) Sedimented Talus: light sediment draping over recognizable talus, substrate has consistently small particle size, (5) Talus: no sediment draping, substrate has consistently small particle size. Special categories were created for less common or challenging bottom types such as fissures, cracks, sheet flows, vent biology, and fault scarps. Defining the extent of sheet flows within the valley was difficult given the level of sediment coverage. Even a light covering of sediment, on the estimated order of tens of centimeters, obscured the edges of sheet flows and prohibited accurate registration. Thus, while these features were identified regularly and assumed to be common throughout flat portions of the valley, the extent of this bottom type was inclusively classified as either unbroken sediment or

sedimented flows. The layers for faults and fissures were not included on the figures due to the relatively fine scale of the individual features. The entire mosaic dataset was classified for geological type by a single observer and the examination order of individual track-line sections for classification was kept random to reduce any regional bias.

2.9 Sources of error

[18] Error accumulation for the geospatial position of pixels throughout the mosaic process limited confidence in the absolute location of sub-meter scale seafloor features. Propagated absolute pixel errors were conservatively estimated as high as 15 meters, while relative errors between consecutive images were less than 2 meters. The ~200 seafloor instrument placements and recoveries provided extensive and redundant coverage of the axial valley and walls; regional trends and substantial features are easily identifiable, and agreement between both consecutive and cross-track images is high (see supplemental materials, Figure B). Additionally, a high degree of correlation exists between topographic features visible in previously collected SM2000 swath bathymetric data [*Johnson et al.*, 2010] and classified bottom types. As an example, all areas classified as talus are co-located with areas of high seafloor slope.

2.10 Interpolation

[19] The linear photo-mosaics and resulting geologic maps were limited in coverage to the specific track-lines taken by the vehicle, resulting in some data gaps between image sets. For purposes of trend identification and statistical evaluation, an interpolation technique was used for gap-filling of geologic classification data. To maintain objectivity and consistency, an iterative nearest neighbor majority interpolation process [*Cover*, 1967] was applied to the entire

classification dataset (Figure 4). The vector classification polygons were rasterized at 0.5 m cell size and cells were given numeric values based on the source polygon's geological classification. The interpolation function consulted all cells within a three cell range and determined the majority class value, then reassigned the subject cell with a matching value. This process added new classified cells to the perimeter of the existing observed survey area. This method projected classification values into un-observed space while preserving 100% of the original observations by ensuring that source cells were re-assigned to their original class values after each iteration. After 15 sequential iterations, the majority of the gaps in the survey area were filled (see supplemental materials, Figure C for additional information). Each cell was also assigned a confidence value between 0 and 100 based on the iteration step that was used for classification; the manually identified cells were given the greatest confidence of 100, decreasing outwards to those classified on iterative step 15, which were given the lowest level of zero confidence (Figure 4).

2.11 Permeability Estimated from Interpreted Seafloor Geology

[20] In order to create a map of relative surface permeability, each of the five major bottom-type classifications was assigned a relative permeability value based on the observed frequency of cracks, voids, openings, and extent of sediment cover. Because of the semi-quantitative nature of our geological interpretations, relative surface permeability was conservatively binned into only three broad categories using the following criteria: (1) High permeability: talus and sedimented talus, (2) Medium permeability: broken flows, (3) Low permeability: sedimented intact pillow basalt flows and unbroken sediment cover without outcrops. In our observations, as relative sediment cover for each bottom class increases, and the occurrence of cracks, fissures,

and gaps between basaltic rocks decreases, the relative permeability of the surface seafloor in our model plausibly decreases. We make this key assumption based on estimations of the vertical hydraulic impedance of a layer of thin sediment [*Karato and Becker*, 1983]. Estimations of sediment depth within regions classified as 'low' permeability were made by assessing the vertical relief of unsedimented and partly sedimented extrusive rock features through comparison with scale references in the images. The vertical relief range of the visible layer of pillow lavas and sheet flows in flat areas is 0.2 to 2.1 meters in over 100 observations, averaging just over 1 meter. In order for this layer of rock to be entirely covered with sediment, as is the case within the valley floor and northern terrace, a blanket of sediment with an average depth of no less than 1 meter would be required. A layer of sediment that is 1 meter thick, with an *in situ* permeability of 10^{-16} m^2, would have a vertical hydraulic impedance of 1.0×10^{16} (1/m). In contrast, a section of Layer 2A with a permeability of 1.8×10^{-10} m^2 to 8.4×10^{-11} m^2 would have a vertical hydraulic impedance of 5.6×10^{9} (1/m) to 1.2×10^{10} (1/m); more than 5 orders of magnitude less than that of the overlying sediment layer. It is critical to stress that this interpretation is limited to only the uppermost visible layer of sediment and geologic structure, providing no ability to project permeability estimates downward into the subsurface.

2.12 Near-bottom water temperature data acquisition

[21] The ROV-mounted SeaBird CTD sensor logged water properties throughout all dives at 1-second intervals. These water property data were filtered to retain only those measurements made between 0.6 and 25 meters of the seafloor. During instrument deployments or other pauses in vehicle motion, heat generated by the ROV electrical systems would be transferred to the water and recorded by the CTD sensor. Filtering all CTD temperatures to remove data when the

vehicle speed dropped below 0.1 meter/second greatly reduced the influence of artificial heating by lack of ROV forward motion.

[22] The water temperature data were also corrected for the decrease in sea water temperatures associated with increasing depth. All ROV CTD water temperature and depth measurements taken during the dives were combined, sorted into 20 meter depth bins, and averaged. A linear regression of water temperature vs depth was calculated from this compilation, since a more complex variation was not justified. All CTD measurements were then corrected for changes in vehicle depth by subtracting the linear regression value, assuming the residual is the temperature anomaly due to near-seafloor heating (see supplemental materials, Figure D). Previous studies have shown that, within the Endeavour axial valley, near-seafloor water parcels can migrate along-axis several hundred meters within a single tidal period [*Garcia-Berdeal et al*., 2006]. Removing this tidal signal for the several-day period of our survey was not possible since no current meter data was available.

2.13 Data Acquisition over Survey Area

[23] The 2011 ROV *JASON II* dive area encompassed in a rectangular area 1 km wide (E-W) and 0.8 km along-strike (N-S) spanning the width of the axial valley and valley walls that included the RAVEN hydrothermal field (Figure 1). Initial photographic coverage of the area of the survey tracklines was estimated at ~48%, while images that passed the filtering processes and were included in the final mosaic represented ~45% of the total area. Average camera altitude for the entire survey was 5.5 meters, with the images used for geological interpretation ranging

from 2.2 to 12.2 meters. The bottom time for the two individual JASON dives at RAVEN was 96 hours and 48 hours.

3. Results

3.2 Geological Description of the Survey Area

[24] Several distinct regions of seafloor geology and sediment coverage exist within the axial valley (Figures 5 and 6). From west to east, the topography of the western wall is uneven and steeply sloped. Normal faults are observed, with exposed scarps extending sub-vertically nearly 50 meters. The most common bottom geological classes on the west wall are talus and broken flows, with islands of scattered sedimented flows in isolated flat areas. A large terrace is located east of the steepest part of the western wall that gently slopes inward toward the center of the axial valley (Figure 5). Topography of this terrace structure ranges from moderately rough in the south to wide and flat at its northern extent. Sediment cover of the seafloor within the terrace is more extensive than on the western wall, and sedimented and broken flows are common with unbroken sediment found primarily to the north. East of the terrace, the seafloor drops steeply to the floor of the axial valley. The transition zone between the terrace and the flat valley floor consists almost entirely of broken flows and talus with only minimal sediment coverage. From the eastern boundary of the talus accumulation derived from the western wall, the flat axial valley floor extends 300 meters to the east and has relatively complete sediment cover and few exposed rock outcrops. The only breaks in the continuous sediment cover of the axial valley floor were cracks, short fissures, and small exposed faults observed in rock outcrops on the

western side of this region, although many of these gaps were at least partially filled with sediment. Across the valley floor, estimated vertical relief from geologic structures averages only 1 m, while fault scarps on the eastern and western ridges can commonly rise abruptly 10 or more meters.

[25] At the eastern edge of the valley floor, the eastern wall rises abruptly and seafloor geology is dominated by small successively higher terraces composed of talus and broken flows interleaved with steep slopes and only minimal sediment cover. Survey tracks are less dense to the east, but show that topography flattens at the summit of the wall and sediment cover increases dramatically, with few exposed rock outcrops. For the entire survey area covered by the photographic images, sedimented flows were the largest single type by area (41%), followed by broken flows (29%), unbroken sediment (21%), and talus (8%), with sedimented talus being the least common (2%). The interpolation process altered the percentage coverage of individual classes by less than 1% from that of the original un-interpolated observations.

3.3 2011 Hydrothermal Vents

[26] Within the RAVEN survey area, a total of 40 individual inactive sulfide mound structures representing fossil vent areas were identified. The majority of these inactive hydrothermal deposits were clustered in groups that were distributed along a roughly linear pattern running NW to SE on the western wall, across the lower terrace, and the western edge of the central valley floor (Figures 5, 6, and 7). Sites of active fluid venting observed in 2011 were restricted entirely to the foot of the west wall. The 16 sites of active venting observed in 2011 were

identified by the presence of vent biology, including tube worms and bacterial mats, shimmering water from diffuse flow, or by sulfide chimneys actively emitting cloudy hydrothermal fluid.

3.4 Hydrothermal Activity from a Previous 2001 Survey

[27] Compilation of video images from the 2001 tn129 *JASON II* cruise to the RAVEN area showed evidence of 18 sites actively venting diffuse low temperature fluid in close proximity to (<20 m) the area imaged in 2011 [*Johnson et al*., 2002]. In contrast, a single chimney emitting high temperature fluid was identified in 2001 with a temperature of 229°C, yet the only high temperature chimney observed in 2011 was located 104 meters to the south of the 2001 high temperature vent site, a distance well outside of any navigational errors. Although the older 2001 high temperature site is still an area of low level fluid emissions, and the inactive 2001 sulfide spire was still visible in 2011, it is clear that the single high temperature fluid emission site within the RAVEN field has migrated over 100 meters along-strike to the south in the 10 years between observations.

3.5 Near-bottom water temperature anomaly

[28] Water temperature anomalies from the processed ROV CTD data ranged from -0.034°C to +0.85°C over the survey area. For the duration of both dives, there was no statistically significant temperature anomaly trend with respect to vehicle altitude within hydrothermal outflow zones ($r < 0.02$). Warm water appeared to be accumulating in the western half of the valley for both dives at RAVEN (Figure 7). The average temperature anomaly for all measurements west of UTMX=493300 was +0.007°, while all measurements to the east averaged -0.006°. All temperature anomalies above the arbitrary threshold value of +0.08°C

were located above the west-wall foot and within 40 meters of an active 2011 fluid emission site. The regions of minimum temperature anomalies were located at the summits of the eastern and western walls, averaging -0.02°C. Negative temperature anomalies are the result of our arbitrary baseline selection and have no physical significance.

4. Interpretation

4.1 Relative surface permeability

[29] The spatial distribution of the simplified three categories of relative permeability mapped over the axial valley show distinct patterns (Figure 8). High surface permeability regions include limited areas on both the eastern and western walls, and the intersection of the valley floor with the west wall. These areas had little to no sediment cover and consisted largely of bare talus blocks and lightly sedimented talus accumulations. The central valley floor, northernmost terrace and summits of the eastern and western valley walls had low relative surface permeability, with nearly complete sediment cover, and few outcrops or surface discontinuities. The southern portion of the terrace and segments of the western-wall foot and valley walls had moderate permeability, and were composed largely of broken flows (Figure 6). The northeast section of the valley floor and northern terrace were classified equally as medium and low surface permeability, with a moderate amount of sediment coverage, more frequent outcrops, and visible cracks present within the seafloor. The axial valley floor is covered with continuous, unbroken sediment cover and may represent a restrictive boundary layer for fluid transmission, as described earlier.

4.2 Bottom water temperature anomalies

[30] An accumulation of anomalously warm bottom water is located over the western half of the axial valley, with the highest temperature anomalies, unsurprisingly, in close proximity to sites of active venting. The eastern half of the valley, including the central valley floor and eastern wall, is the area with the lowest temperature anomalies and has no active vents. The noticeable agreement between the locations of highest temperature anomalies and observed active vents strongly supports the conclusion that warm fluid is only being discharged on the western side of the axial valley within the RAVEN area, specifically along the foot of the western wall. While the shoaling of the magma lens on the western side of the valley seems the most likely cause of the position of the warm water pool, it is worthwhile to note that the highest water temperature anomalies also appear above a region mapped as having high seafloor permeability.

4.3 Location of vents

[31] In 2011, all active and almost all fossil fluid vent sites were found at the foot of the west wall. Several previous studies have observed that the partial melt zone of the axial magma chamber along the Endeavour Segment of the Juan de Fuca ridge shoals on the western edge of the valley, rising up to 400 hundred meters closer to the seafloor than on the eastern side [*Van Ark et al*., 2007; *Wilcock et al*., 2009; *Kelley et al*., 2012]. The shoaling of the roof of the magma lens beneath the western portion of the RAVEN field may largely explain why the majority of active and fossil structures are located on the western half of the axial valley, as circulation upflow should be enhanced where the vertical thermal gradient is steepest. The observation that all current or recently active vents are located within the zones of relatively high upper surface permeability, while most fossil sulfide structures appear in zones classified as low

permeability, may suggest that sediments that accumulate across low relief sections of the axial valley could eventually restrict the relatively low intensity fluid outflow zones.

4.4 Spatial Distribution of Relative Permeability

[32] Within the axial valley at RAVEN, our estimation of relative upper surface permeability is largely controlled by the extent of sediment cover, which appears correlated with the slope and roughness of the underlying seafloor. Regions of low topographic slope and smooth terrain capture and retain sediment cover that is observably thicker and more spatially continuous, while steeper and rougher regions of the seafloor accumulate little sediment, which is likely transported downslope. It is important to note that while the vertical non-hydrothermal sediment flux is assumed to be roughly uniform across the valley, the accumulation rate appears heavily biased by topography. In regions with rough and uneven topography with relief greater than several meters, the underlying extrusive rocks with high porosity and presumed high relative permeability are directly exposed to the seawater. In these uneven regions of low sediment accumulation, the uppermost veneer of the seafloor appears to provide little resistance for fluid entering or leaving the sub-surface fluid reservoir. In contrast, even within the youngest crust of the central axial valley, seafloor with smooth basement topography and relief of the order of 1 meter rapidly accumulates a complete and unbroken layer of sediment. This sedimentation is presumably partially derived from mineral precipitation and intense biological activity associated with hydrothermal fluid emission, and originates from active vent sites located throughout the Endeavour axial valley. This sediment not only accumulates on the axial valley floor, but is also redistributed by tidally-driven bottom currents over the valley walls, terraces and the top of the summit ridges [*Hautala et al*., 2005]. This migration of sediments both downslope and

horizontally throughout the axial valley may also contribute to re-deposition on the smallest scale; accumulating within local topographic depressions, open fissures, and in gaps between individual pillow basalt extrusions; consequently gradually reducing the permeability of the surface veneer locally with increasing time.

[33] The influence of surface permeability can also be examined in terms of predicted fluid flow velocity using a simple formulation of Darcy's law:

$$\mathrm{v} = -\frac{1}{\eta\phi} k \cdot \nabla P$$

Where 'v' is predicted fluid velocity, 'η' is fluid viscosity, 'ϕ' is porosity, and 'k' is permeability, and '∇P' is the pore pressure gradient. Taking the porosity of the lavas and sediment to be of the same order, and keeping both the fluid viscosity and pressure gradient forces constant, fluid flow velocity through the sediment layer should be far slower than through the lavas, regardless of direction. The weakly buoyant diffuse hydrothermal fluid (rather than the focused high temperature upflow) could flow horizontally to the nearby openings in the surface veneer more readily than penetrating even the thin overlying sediment cap.

[34]Tectonic activity caused by continued sea floor spreading and magma injection from below will modify the distribution of faults, fissures and morphology within the axial valley [*Wilcock et al.*, 2002]. Each new cycle of tectonic or magmatic activity could 'reset' the spatial distribution of surface layer permeability within the axial valley, redistribute portions of the mobile sediment

cover, and relocate both fluid emission and seawater recharge sites for the sub-surface crustal reservoir.

[35] The eastern and western valley walls and the talus accumulations at the foot of the western wall are the primary regions of high relative upper surface permeability, while the lowest surface permeability was restricted to the central valley floor and northern terrace (Figure 6). Within 40 meters of active vent sites, relative surface permeability is high and sediment cover is presently sparse. At a distance of approximately 100 meters from active vent sites, we observed a predominance of low surface permeability zones and an abundance of relatively thick sediment cover. Cracks and larger fissures are far more common in the areas adjacent to active fluid vent sites, although there is evidence that many of these are partially or completely filled with sediment (see supplemental materials, Figure E).

5. Conclusions

[36] Our observations suggest a revised hydrothermal circulation model where the permeability of the upper surface veneer of the seafloor of the axial valley is a time-dependent and evolving primary boundary condition for fluid flux into and out of the subsurface hydrothermal reservoir (Figure 9). The spatial definition of this proposed boundary condition is dependent on photographic observations, and therefore interpretations are restricted to only the uppermost surface veneer of the seafloor. Almost all of the geological features and processes primarily responsible for driving and controlling ridge axis hydrothermal fluid circulation, such as magma chamber location and depth, normal and listric faults that penetrate deep within the crust, and chemical alteration and precipitation zones, are clearly hidden from the ROV video camera.

However, the warm hydrothermal fluid that is emitted, or the cold seawater that is recharging the sub-surface crustal reservoir, must still pass through this thin surface interface, making the visible seafloor the location of critical access ports for mid-ocean ridge hydrothermal fluid circulation. Additional experiments could be conducted at RAVEN to test the observations made in this study. Direct *in situ* measurements of sediment permeability and thickness would provide the additional critical parameters for numerical models. Direct measurements of fluid flux at the seawater/sediment/basement interface would quantify fluid flow rates across the veneer. Finally, mapping the surface conductive heat flow will help characterize the structure of any fluid circulation cells within Layer 2A, providing the link between surface permeability and fluidre-charge or emission, a study that is presently underway.

Acknowledgments

[37] Support for this project was provided by NSF Grant 1230102 to H. P. Johnson. The crew of the R/V *Atlantis* and operating crew of the ROV *Jason II* were integral to the success of this study. Personal communications with Maurice Tivey, Javier Escartín, Susan Hautala, Miles Logsdon, Mike Hutnak and Marie Salmi were instrumental in the completion of this research. Special thanks are given to Baxter Hutchinson of the ROV *Jason II* for providing technical specifications for the vehicle and camera system, and Scott McCue at WHOI for his patience and advice.

References

Barreyre, T. and Escartin, J., R. Garcia, M. Cannat, E. Mittelstaedt, and R. Prados (2012), Structure, temporal evolution, and heat flux estimate from the Lucky Strike deep-sea hydrothermal field derived from seafloor image mosaics, *Geochem. Geophys. Geosyst.*, *13*, Q04007, doi:10.1029/2011GC003990.

Bouguet, J.-Y., and P. Perona (1998), 3D photography on your desk, in Computer Vision: Fifth European Conference on Computer Vision, edited by H. Burkhardt and B. Neumann, pp. 43–50, Springer, Berlin. (Available at http://www.vision.caltech.edu/bouguetj/calib_doc/)

Carlson, R. L. (2011), The effect of hydrothermal alteration on the seismic structure of the upper oceanic crust: Evidence from Holes 504B and 1256D, *Geochem. Geophys. Geosyst.*, *12*(9), doi:10.1029/2011GC003624.

Childress, J. J., and C. R. Fisher (1995), The biology of hydrothermal vent animals: physiology, biochemistry, and autotrophic symbioses, *Oceanogr. Mar. Biol. Ann. Rev., 30*, 337-441.

Coumou, D., T. Driesner, and C. A. Heinrich (2008), The Structure and Dynamics of Mid-Ocean Ridge Hydrothermal Systems, *Science, 321*, 1825-1828, doi:10.1126/science.1159582.

Cover, T., & Hart, P. (1967), Nearest neighbor pattern classification. *Information Theory, IEEE Transactions on*, *13*(1), 21-27.

Escartín, J., et al. (2008), Globally aligned photomosaic of the Lucky Strike hydrothermal vent field (Mid-Atlantic Ridge, 37_18.50N): Release of georeferenced data, mosaic construction, and viewing software, *Geochem. Geophys. Geosyst.*, *9*, Q12009, doi:10.1029/2008GC002204.

Garcia-Berdeal, I., S. L. Hautala, L. N. Thomas, and H. P. Johnson (2006), Vertical structure of time-dependent currents in a mid-ocean ridge axial valley. *Deep Sea Research Part I: Oceanographic Research Papers, 53*(2), 367-386.

Giambalvo, E. R., A. T. Fisher, J. T. Martin, L. Darty, and R. P. Lowell (2000). Origin of elevated sediment permeability in a hydrothermal seepage zone, eastern flank of the Juan de Fuca Ridge, and implications for transport of fluid and heat, *J. Geophsy. Res., 105,* B1, 913-928.

Gilbert, L. A., and H. P. Johnson (1999), Direct measurements of oceanic crustal density at the northern Juan de Fuca Ridge, *Geophys. Res. Lett., 26*(24), 3633–3636, doi:10.1029/1999GL008391.

Hautala, S. L., Johnson, H. P., & Bjorklund, T. (2005). Geothermal heating and the properties of bottom water in Cascadia Basin. *Geophys. Res. Lett., 32*(6), L06608.

Holmes, M. L., and H. P. Johnson (1993), Upper crustal densities derived from sea floor gravity measurements: northern Juan de Fuca ridge, *Geophys. Res. Let., 20*, 1871-1874

Hutnak,M., A. T. Fisher, L. Zühlsdorff, V. Spiess, P. H. Stauffer, and C. W. Gable (2006), Hydrothermal recharge and discharge guided by basement outcrops on 0.7–3.6 Ma seafloor east of the Juan de Fuca Ridge: Observations and numerical models, *Geochem. Geophys. Geosyst., 7,* Q07O02, doi:10.1029/2006GC001242.Johnson, H. P., K. Becker, and R. V. Herzen (1993), Near-axis heat flow measurements on the northern Juan de Fuca Ridge: Implications for fluid circulation in oceanic crust, *Geophys. Res. Lett., 20,* 1875-1878, doi: 0094-8534/93/93 GL-00734503.00.

Johnson, H. P., Pruis, M. J., Van Patten, D., & Tivey, M. A. (2000), Density and porosity of the upper oceanic crust from seafloor gravity measurements, *Geophys. Res. Lett.*, *27*(7), 1053-1056.

Johnson, H. P., S. L. Hautala, M. A. Tivey, C. D. Jones, J. Voight, M. Pruis, I. Garcia-Berdeal (2002), Survey studies hydrothermal circulation on the northern Juan de Fuca Ridg, *Eos, Transactions American Geophysical Union. 83*, no. 8 73.

Johnson, H. P., M. A. Tivey, T. A. Bjorklund, and M. S. Salmi (2010), Hydrothermal circulation within the Endeavour Segment, Juan de Fuca Ridge, *Geochem. Geophys. Geosyst.*, *11*, Q05002, doi:10.1029/2009GC002957.

Karato, S.-I., and K. Becker (1983), Porosity and hydraulic properties of sediments from the Galapagos spreading center and their relationship to hydrothermal circulation in the oceanic crust, *J. Geophys. Res*., 88, 1009-1017.

Langseth, M. G., Becker, K., Von Herzen, R. P., and P. Schultheiss (1992), Heat and fluid flux through sediment on the western flank of the Mid-Atlantic Ridge: a hydrogeological study of North Pond, *Geophys. Res. Lett.*, 19, 517-520.

Lessard-Pilon, S., M. D. Porter, E. E. Cordes, I. MacDonald, and C. R. Fisher (2010), Community composition and temporal change at deep Gulf of Mexico cold seeps, *Deep-Sea Res. II, 57,* 1891-1903, doi:10.1016/j.dsr2.2010.05.012.

Lister, C.R.B. (1972), Thermal balance of a mid-ocean ridge, *Geophys. J. R. Astron. Soc.*, *26*, 515-535, doi: 10.1111/j.1365-246X.1972.tb05766.x.

Lowell, R. P., Y. Yao, and L. N. Germanovich, (2003), Anhydrite precipitation and the relationship between focused and diffuse flow in seafloor hydrothermal systems, *J. Geophys. Res.*, *108*, B9, doi: 10.1029/2002JB002371.

Lowell, R.P., A. Farough, L.N. Germanovich, L.B. Hebert, and R. Horne (2012), A vent-field-scale model of the East Pacific Rise 9°50'N magma-hydrothermal system, *Oceanography, 25*(1), 158–167, http://dx.doi.org/10.5670/oceanog.2012.13.

Mittelstaedt, E., J. Escartín, N. Gracias, J.-A. Olive, T. Barreyre, A. Davaille, M. Cannat, and R. Garcia (2012), Quantifying diffuse and discrete venting at the Tour Eiffel vent site, Lucky Strike hydrothermal field, *Geochem. Geophys. Geosyst.*, *13*, Q04008, doi:10.1029/2011GC003991.

Nedimović, M. R., Carbotte, S. M., Diebold, J. B., Harding, A. J., Canales, J. P., and Kent, G. M. (2008), Upper crustal evolution across the Juan de Fuca ridge flanks, *Geochem. Geophys. Geosyst., 9*(9), doi:10.1029/2008GC002085.

Newman, K. R., Nedimović, M. R., Canales, J. P., & Carbotte, S. M. (2011), Evolution of seismic layer 2B across the Juan de Fuca Ridge from hydrophone streamer 2-D traveltime tomography, *Geochem. Geophys. Geosyst., 12*(5), doi:10.1029/2010GC003462.

Pruis, M. J., and H. P. Johnson (2004), Tapping into the sub-seafloor: examining diffuse flow and temperature from an active seamount on the Juan de Fuca Ridge. *Earth and Planetary Science Letters 217.3*: 379-388.

Rabinowicz, M., J.-C. Sempere, and P. Genthon (1999), Thermal convection in a vertical permeable slot: Implications for hydrothermal circulation along mid-ocean ridges, *J. Geophsy. Res., 104,* 29275-29292, doi: 0148-0227/99/1999JB900259509.00.

Robigou, V., J. R. Delaney, and D. S. Stakes (1993), Large massive sulfide deposits in a newly discovered active hydrothermal system the High-Rise field, Endeavour segment Juan de Fuca Ridge, *Geophys. Res. Lett., 20,* 1887-1890

Salmi, M., M. Hutnak, C. Hearn, M. Tivey, T. Bjorklund, H. P. Johnson (2012), Characterization of Active Hydrothermal Fluid Discharge and Recharge Zones in the Endeavour Axial Valley, Juan de Fuca Ridge, Abstract OS13D-1761 presented at 2012 Fall Meeting, AGU, San Francisco, Calif., 3-7 Dec.

Spinelli, G. A., E. R. Giambalvo, and A. T. Fisher (2004), Sediment permeability, distribution, and influence on fluxes in oceanic basement, *Hydrogeology of the oceanic lithosphere*, 151-188.

Stein, C., and S. Stein (1992), A model for the global variation in oceanic depth and heat flow with lithospheric age, *Nature*, *359*, 123-129, doi: 10.1038/359123a0.

Stein, C., and S. Stein (1994), Constraints on hydrothermal heat-flux through the oceanic lithosphere from global heat-flow, *J. Geophys. Res.*, *99,* 3081-3095, doi: 10.1029/93JB02222.

Tivey, M. A., and H. P. Johnson (2002), Crustal magnetization reveals subsurface structure of Juan de Fuca Ridge hydrothermal vent fields. *Geology* 30.11: 979-982.

Tolstoy, M., F. Waldhauser, D. R. Bohnenstiehl, R. T. Weekly, and W.-Y. Kim (2008), Seismic identification of along-axis hydrothermal flow on the East Pacific Rise, *Nature, 451*, 181–184, doi:10.1038/nature06424.

Van Ark, E. M., R. S. Detrick, J. P. Canales, S. M. Carbotte, A. J. Harding, G. M. Kent, M. R. Nedimovic, W. S. D. Wilcock, J. B. Diebold, and J. M. Babcock, (2007), Seismic structure of the Endeavour Segment, Jaun de Fuca Ridge: Correlations with seismicity and hydrothermal activity, *J. Geophys. Res., 112,* B02401, doi:10.1029/2005JB004210.

Wilcock, W. S. D., (1998), Cellular convection models of mid-ocean ridge hydrothermal circulation and the temperatures of black smoker fluids, *J. Geophys. Res.*, *103*, B2, 2585-2596

Wilcock, W. S. D., S. D. Archer, and G. M. Purdy (2002) Microearthquakes on the Endeavour segment of the Juan de Fuca Ridge. *J. Geophys. Res., 107*, B12, EPM 4-1-EPM4-21, doi: 10.1029/2001JB000505.

Wilcock, W. S. D., E. E. E. Hooft, D. R. Toomey, P. R. McGill, A. H. Barclay, D. S. Stakes, and T. M. Ramirez (2009), The role of magma injection in localizing black-smoker activity, *Nature Geosci.*, *2*, 509-513, doi: 10.1038/NGEO550.

Williams, D. L., K. Green, T. H. van Andel, R. P. Von Herzen, J. R. Dymond, and K. Crane (1979), The hydrothermal mounds of the Galapagos Rift: Observations with DSRV *Alvin* and detailed heat flow studies, *J. Geophys. Res*., 84, 7467–7484.

Wolery, T.J., and N.H. Sleep (1976), Hydrothermal circulation and geochemical flux at mid-ocean ridges, *J. Geology*, *84*, 249-275.

Figure Captions

Figure 1

The study location is depicted in relation to three other well-studied sites along the Endeavour Segment of the Juan de Fuca ridge. The RAVEN vent field (pink) is shown south of High Rise and Clam Bed, and north of Main Endeavour. The extent of the 2011 ROV image survey is shown in purple. Bathymetric data were obtained via SM2000 multibeam sonar [*Tivey and Johnson*, 2002; *Johnson et al*., 2010] with contour lines shown every 10 meters.

Figure 2

The mosaic workflow initiated (top of figure) with geo-referencing of image extents, followed by blending of image edges to create a seamless mosaic, and concluded (bottom of figure) by drawing classification polygons over identifiable homogenous bottom features to generate the original geologic map.

Figure 3

The bottom class and permeability designations for geologic features are listed by attribute. Example images of each bottom class are shown with designations for sediment cover, substrate type, cracks, slope, and relative permeability. Image properties were altered to improve contrast consistent with the mosaics at the time of examination. Percent coverage of the study area for each bottom class is also listed.

Figure 4

The interpolation procedure used for figures 6 and 8 was designed to maximize coverage while preserving the integrity of the original observations. All panels cover the same geographic area. Panel A shows the geologic map before interpolation. Panel B shows the interpolated geologic map. The area shown in black is ‘no data’ and is reduced in size during the interpolation process. All colored regions are classified observations of the seafloor. Panel C shows the confidence heat-map of the interpolation iterations, starting with the highest confidence at the track line (red, confidence = 100) and ending with the 15^{th} iteration (pink, confidence = 0). The area depicted is from the northeast corner of the study site, spanning 140 meters North-South and 220 meters East-West.

Figure 5

E-W bathymetric profile across the RAVEN axial valley at 47°57’10’’ N, through the active vent region. Designated geographical regions are indicated. Total vertical relief is ~120 meters.

Figure 6

The interpolated geologic map showing the 5 dominant bottom classifications. Colored polygons correspond to bottom classes listed in the legend. SM2000 Bathymetry was interpolated using an Inverse Distance Weighted (IDW) technique and extracted 10 meter contours are shown behind polygons. Active and inactive vents are depicted as white and black triangles.

Figure 7

The interpolated bottom water temperature anomaly from ROV CTD data was gridded at 10 meters and ranged from -.02° to 0.8°C. Contours at .01°C intervals are shown above the interpolated bottom water temperature grid. The warm pool over the western half of the axial valley is clearly visible (yellow region), with the highest anomaly regions in close proximity to active vent sites.

Figure 8

The inferred permeability data is depicted as a three-class relative permeability map. SM2000 Bathymetry was interpolated using an Inverse Distance Weighted technique and extracted 10 meter contours are shown behind polygons. 2011 active and inactive vents are shown above active 2001 vents as colored triangles. Regions of high and medium permeability are clearly visible around active vents, with low permeability regions farther away. The eastern and western walls are both visible in the bathymetry and characterized by moderate to high permeability.

Figure 9

A cartoon of our revised subsurface fluid reservoir model. A thin veneer caps the subsurface layers with occasional entry and exit regions of high permeability. Within the veneer, a 1 meter layer of sediment (black) with an estimated permeability of 10^{-16} m^2 would resist fluid flow far more than unsedimented rock (white) with a permeability of 10^{-11} m^2. Layer 2A is shown beneath the cap, extending to a depth of 350 m. The bulk permeability of this layer is low, but anisotropy is high. The location of fluid conduits such as open faults and fissures within this layer would greatly influence fluid pathways; however, the low bulk permeability would allow for high fluid flow at many locations. Layer 2B’s interface with Later 2A is visible as a transition from porous, low density extrusives to lower porosity and greater density vertical dikes. Approximate velocity, porosity, and permeability values shown are taken from *Newman et al*. [2011], *Nedimović et al*. [2008], *Carlson* [2011], and *Johnson et al*. [2000].

Figures

Figure 1

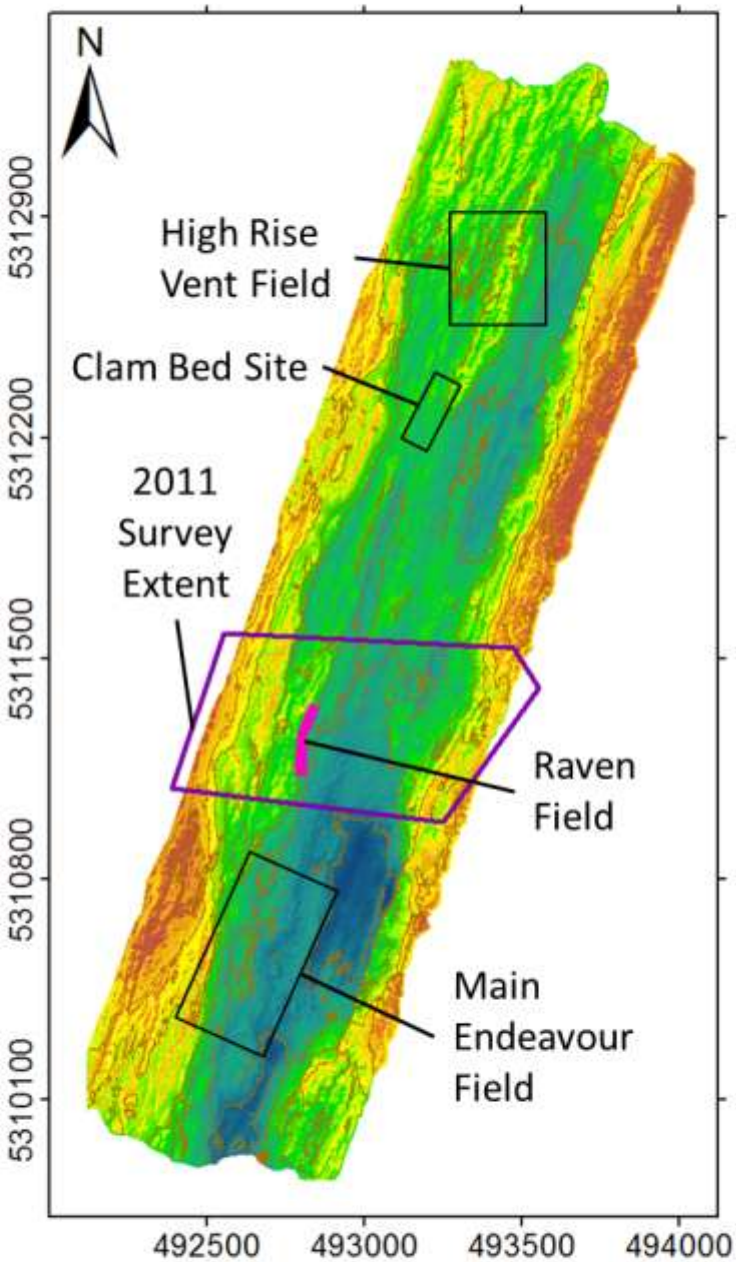

Figure 2

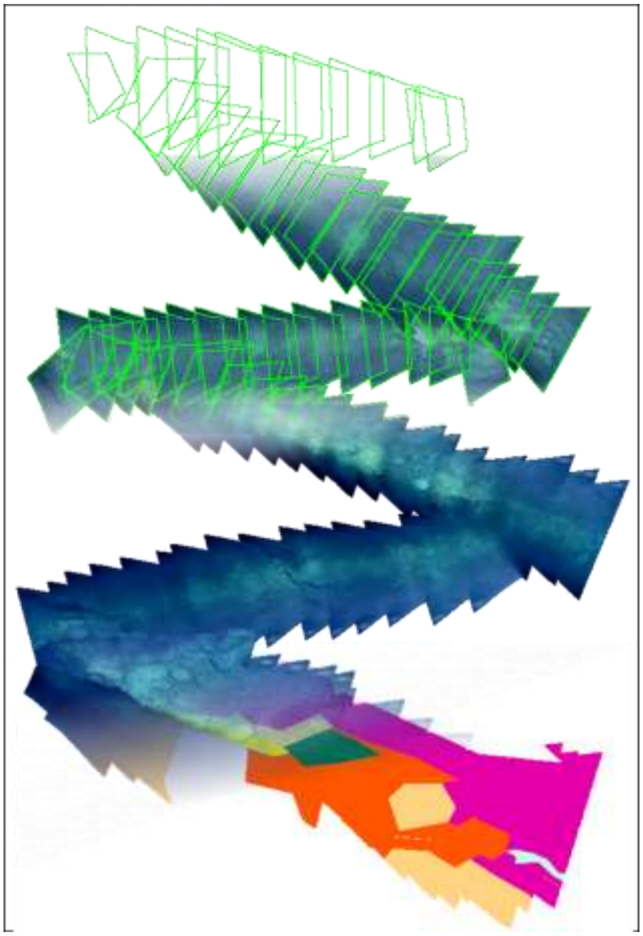

Figure 3

Bottom Class	Unbroken Sediment	Sedimented Flows	Broken Flows	Sedimented Talus	Talus
Sediment Cover	thick	light-thick	none-light	light	none
Substrate	not visible or not identifiable	recognizable	loosly assorted, varying shapes & sizes	small particle size	small particle size
Cracks	none	small	small openings	in-filled (none visible)	in-filled (none visible)
Slope	low	low	low-moderate	high	high
Example Image					
Permeability	Low	Low	Med	High	High
% Coverage	21	41	29	2	8

Figure 4

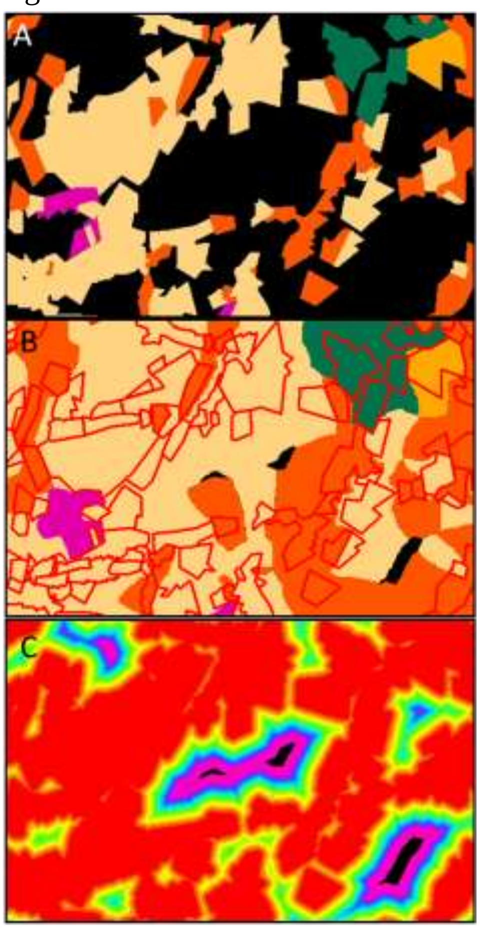

Figure 5

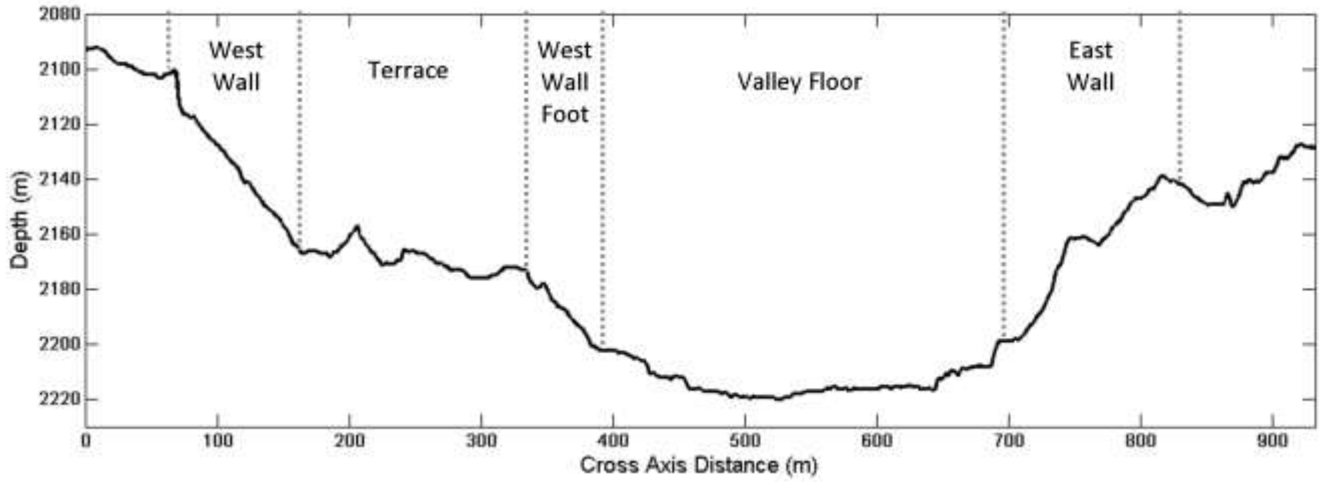
West
Wall
Terrace
West
Wall
Foot
Valley Floor
East
Wall
Depth (m)
Cross Axis Distance (m)
2080
2100
2120
2140
2160
2180
2200
2220
0
100
200
300
400
500
600
700
800
900

Figure 6

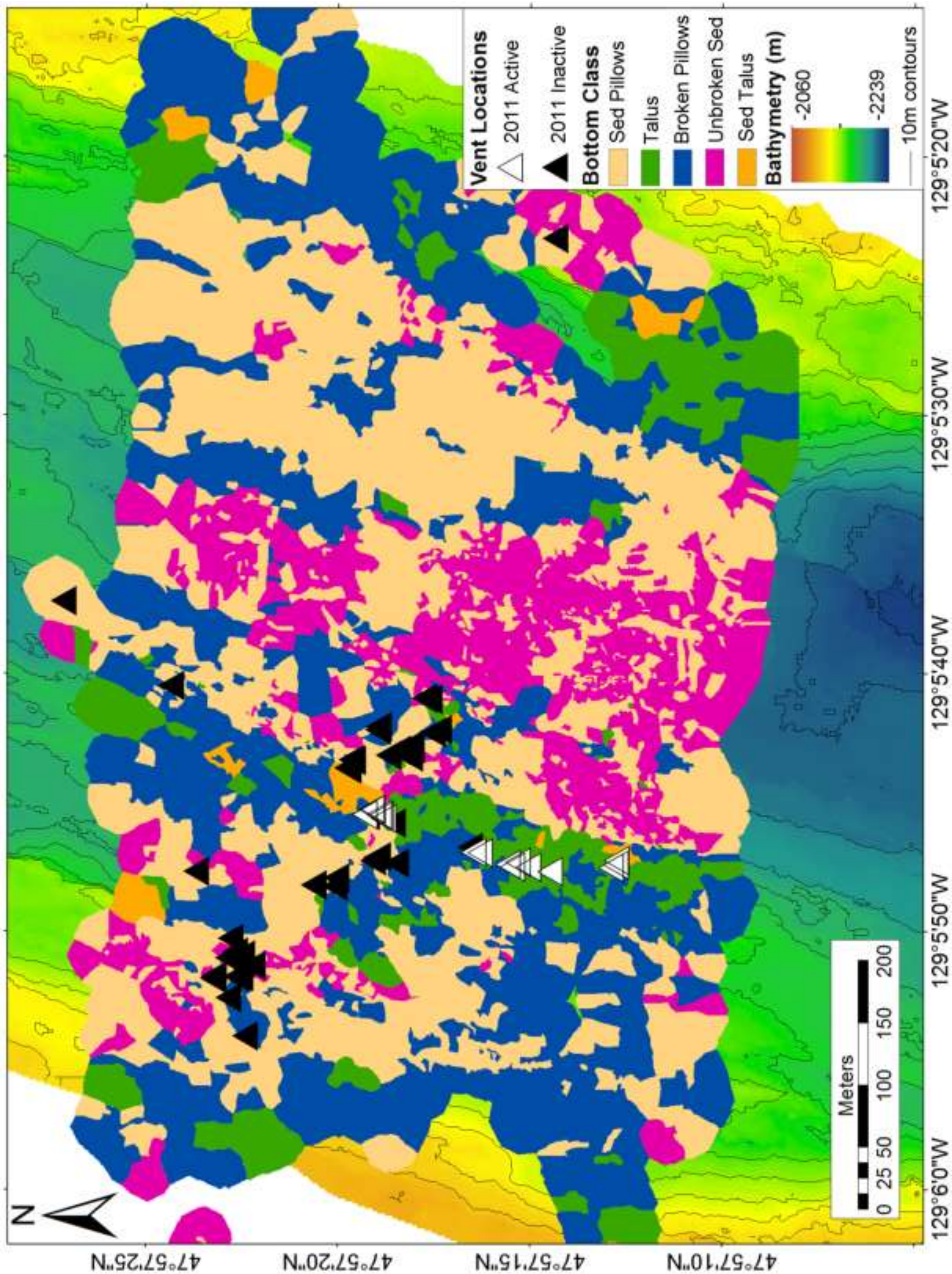
Vent Locations
2011 Active
2011 Inactive
Bottom Class
Sed Pillows
Talus
Broken Pillows
Unbroken Sed
Sed Talus
Bathymetry (m)
-2060
-2239
10m contours
129°5'20"W
129°5'30"W
129°5'40"W
129°5'50"W
129°6'0"W
47°57'25"N
47°57'20"N
47°57'15"N
47°57'10"N
Meters
0 25 50 100 150 200
N

Figure 7

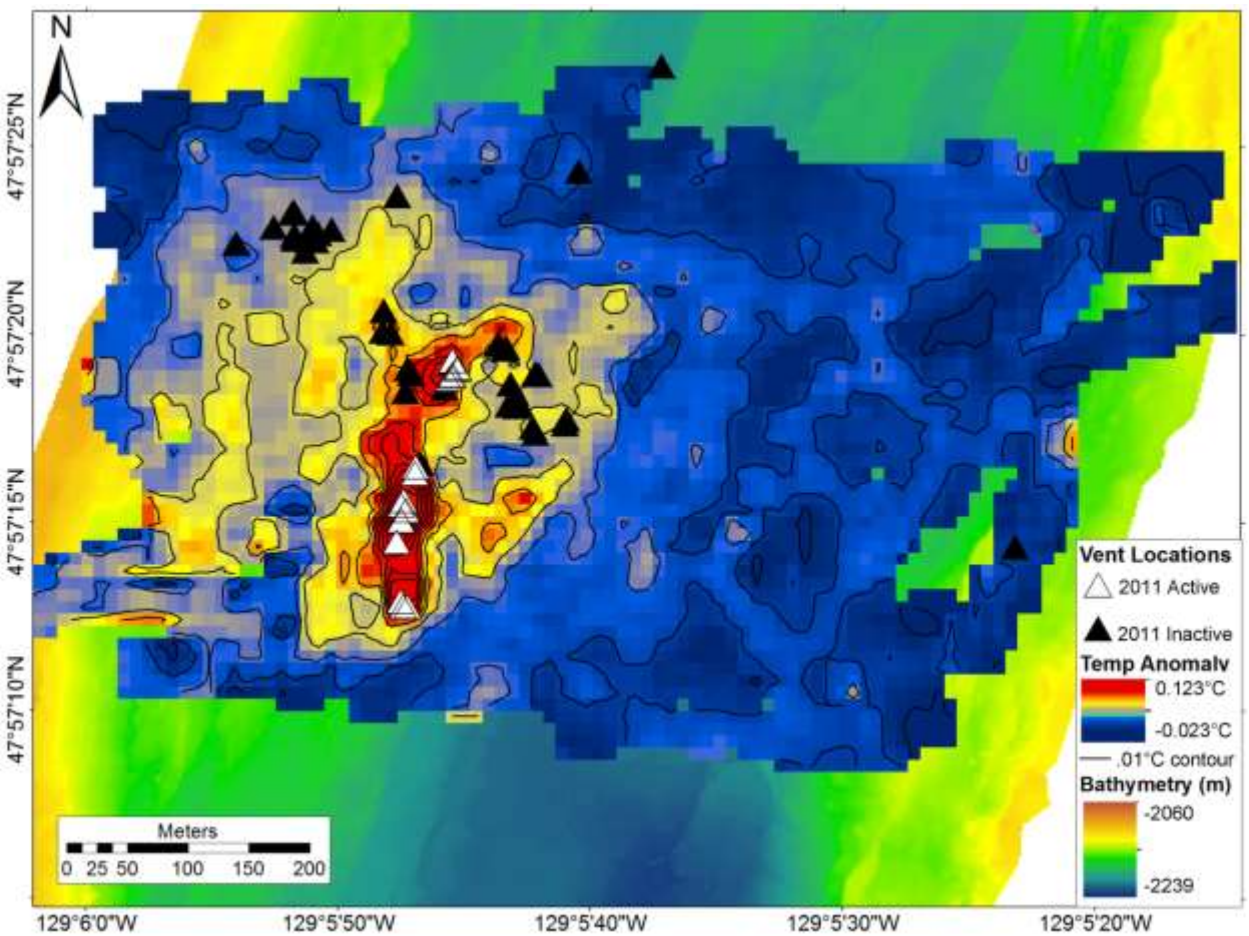
N
47°57'25"N
47°57'20"N
47°57'15"N
47°57'10"N
129°6'0"W
129°5'50"W
129°5'40"W
129°5'30"W
129°5'20"W
Meters
0 25 50 100 150 200
Vent Locations
2011 Active
2011 Inactive
Temp Anomaly
0.123°C
-0.023°C
.01°C contour
Bathymetry (m)
-2060
-2239

Figure 8

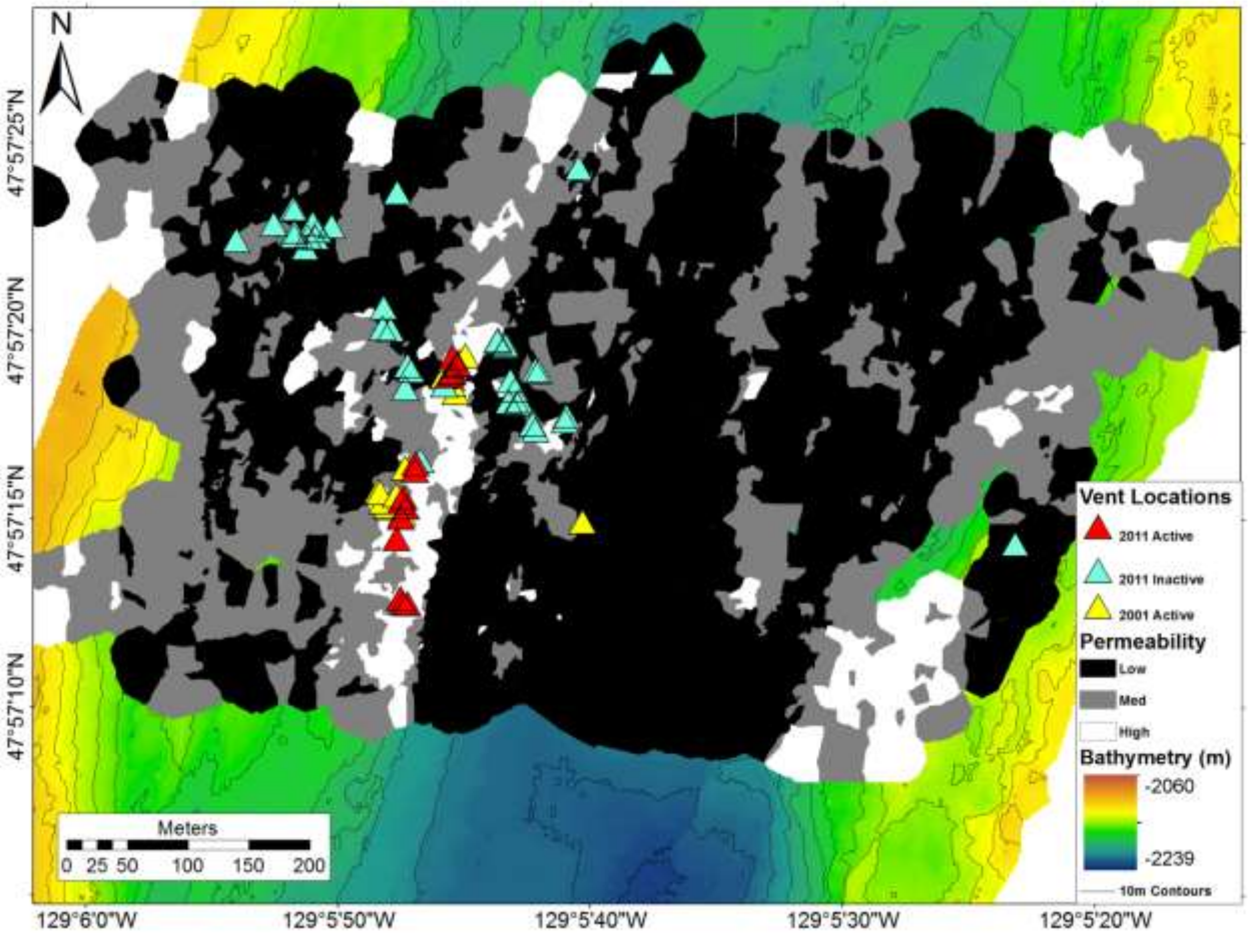
N
47°57'25"N
47°57'20"N
47°57'15"N
47°57'10"N
129°6'0"W
129°5'50"W
129°5'40"W
129°5'30"W
129°5'20"W
Meters
0 25 50 100 150 200
Vent Locations
2011 Active
2011 Inactive
2001 Active
Permeability
Low
Med
High
Bathymetry (m)
-2060
-2239
10m Contours

813 Figure 9

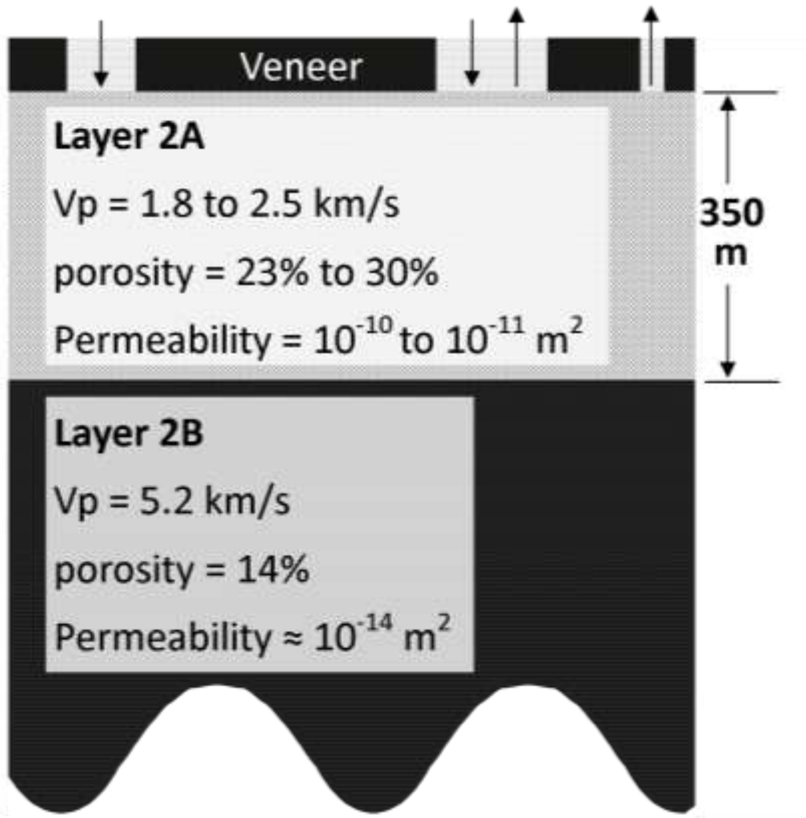

814
815

Supplemental Material

Appendix A: Image Geo-referencing Details

Figure A

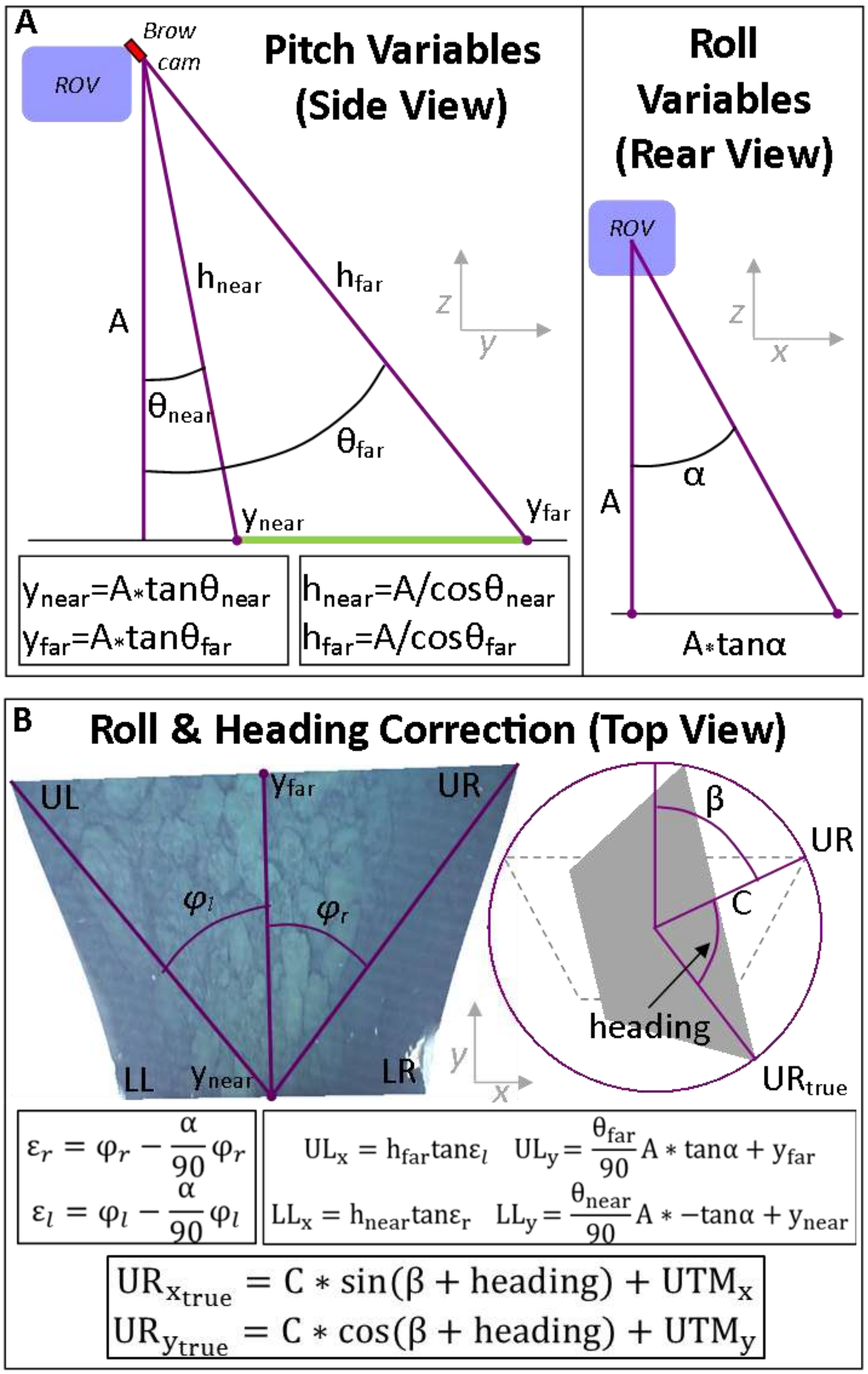

Panel A shows the derivation of along-axis and lateral extent for each image, related to vehicle pitch and roll as well as camera angle and coverage. Panel B shows the calculation of corner coordinates, image rotation to account for vehicle heading, and coordinate conversion to UTM. Images were then integrated to the mosaic as depicted in Fig 2.

Appendix B: Supporting Images

Figure B

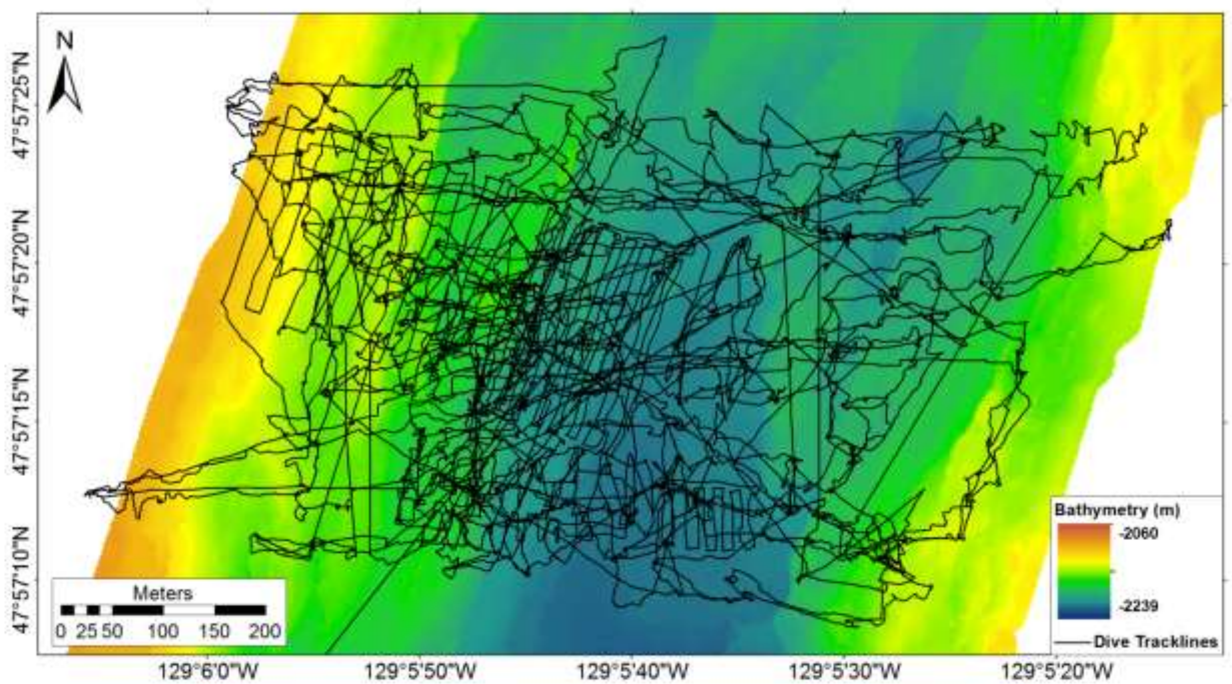

The ROV track lines for dives 586 and 590 are shown above bathymetry. The track lines exceed the extent of the classified image mosaic due to unusable images obtained during high-altitude transit.

Figure C

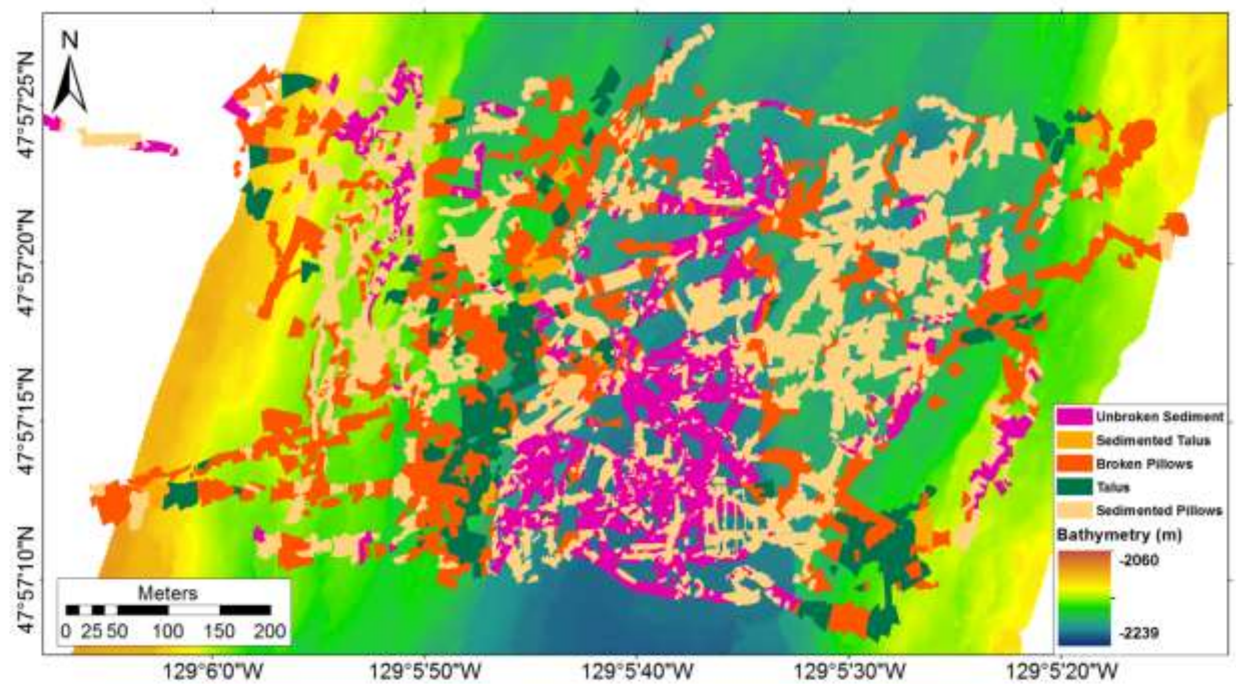

The original bottom class polygons for the five dominant bottom types are shown here above bathymetry. The interpolation process filled in gaps between observations (Figures 4 and 6).

Figure D

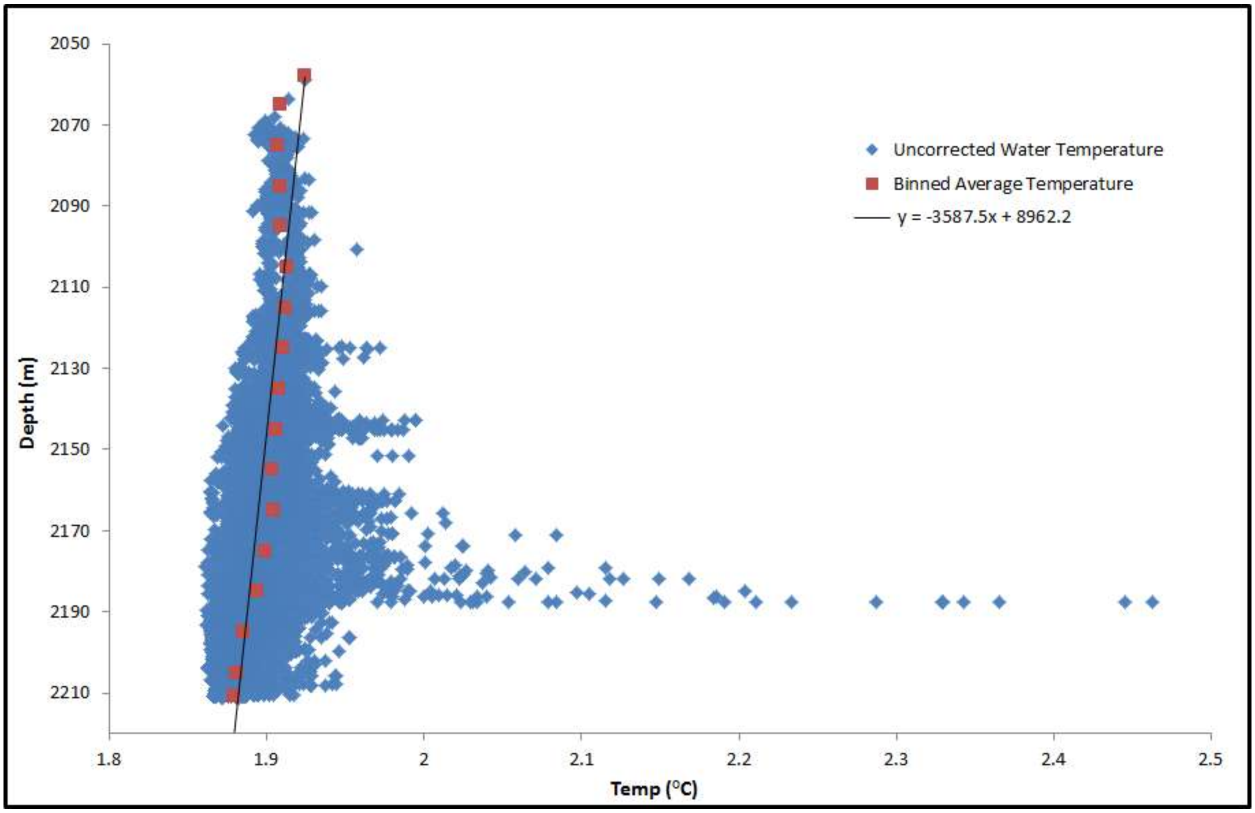

The near-bottom water temperature correction process. Temperature measurements were first binned by depth before an average value was obtained for each bin. The linear regression is calculated using the bin averages. The regression line was used to normalize the water temperature dataset for the depth trend. Measurements were far more numerous near the bottom, and a regression line through the un-binned temperatures yields a distorted depth trend (biased by the high temperatures surrounding the vents). The bin method provided a far more reliable estimate of the background depth-temperature relationship.

Figure E

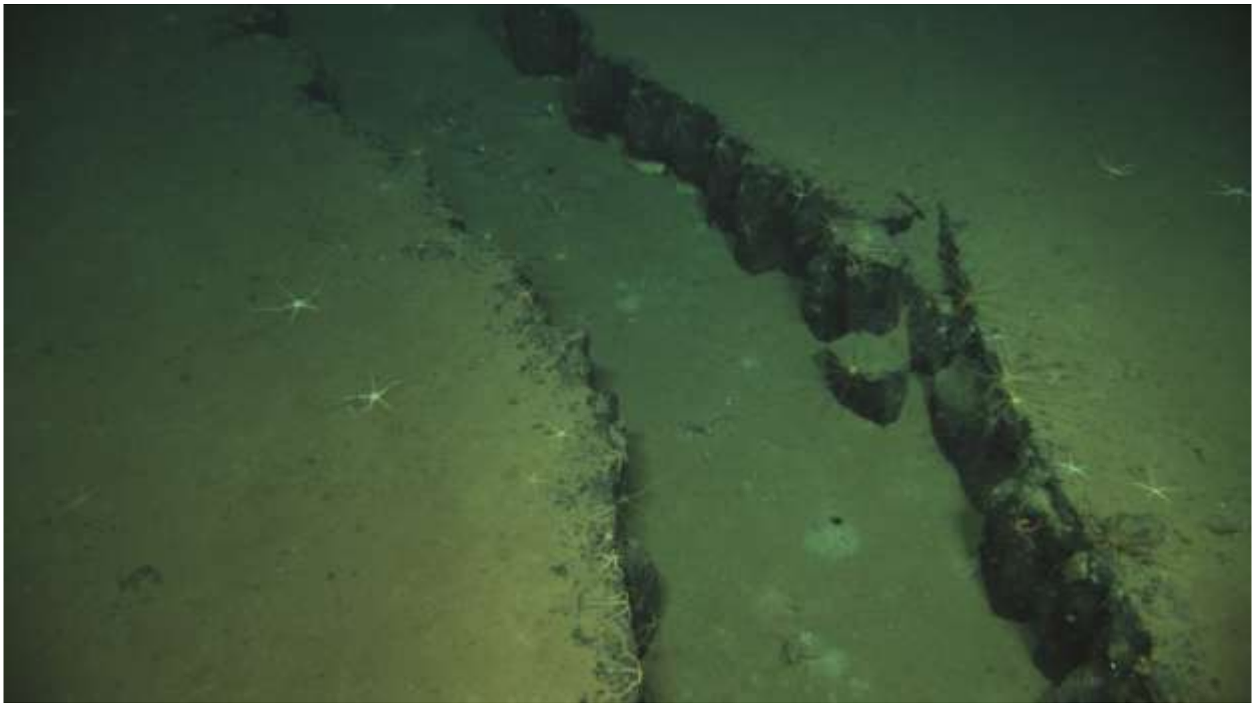

Example image of a typical fissure encountered during a traverse of the central axial valley floor. This feature is approximately 1 to 1.5 meters across and runs for over 80 meters uninterrupted out of the camera’s field of view. The fissure is almost completely filled with sediment, possibly negating the chance of it acting as a conduit for fluid flow.

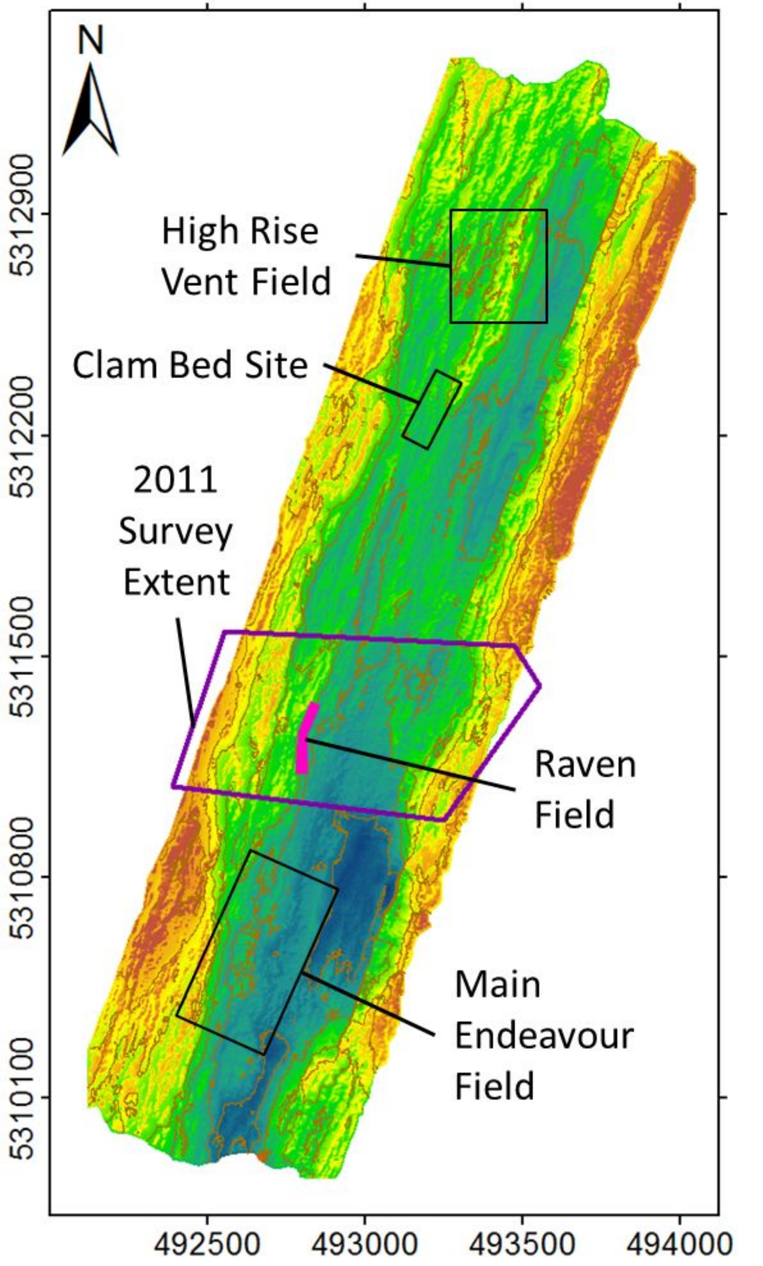
N
High Rise
Vent Field
Clam Bed Site
2011
Survey
Extent
Raven
Field
Main
Endeavour
Field
5312900
5312200
5311500
5310800
5310100
492500
493000
493500
494000

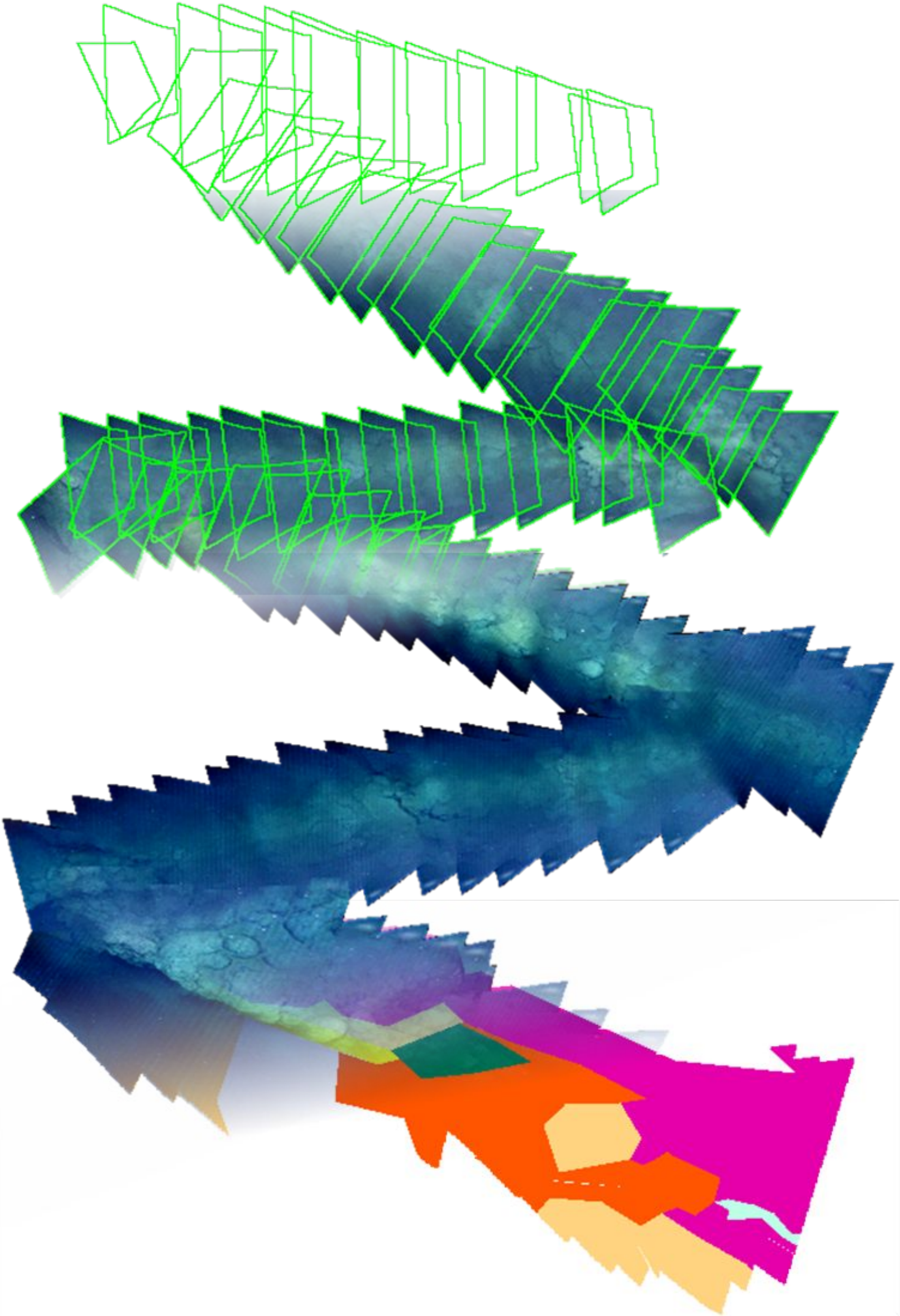

Bottom Class	Unbroken Sediment	Sedimented Flows	Broken Flows	Sedimented Talus	Talus
Sediment Cover	thick	light-thick	none-light	light	none
Substrate	not visible or not identifiable	recognizable	loosly assorted, varying shapes & sizes	small particle size	small particle size
Cracks	none	small	small openings	in-filled (none visible)	in-filled (none visible)
Slope	low	low	low-moderate	high	high
Example Image	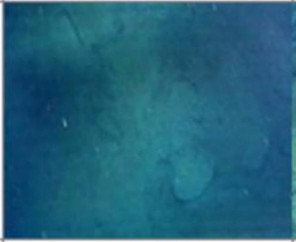	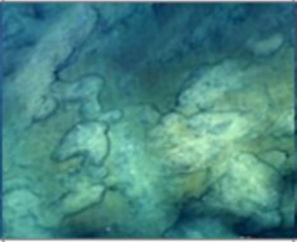	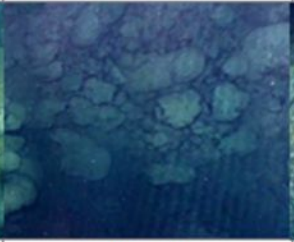		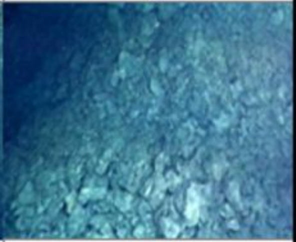
Permeability	Low	Low	Med	High	High
% Coverage	21	41	29	2	8

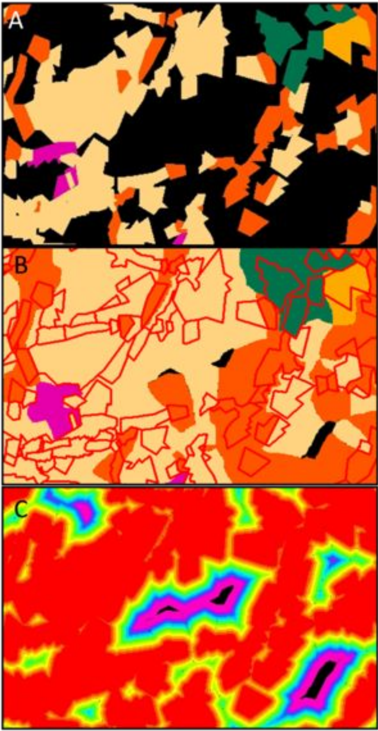
A
B
C

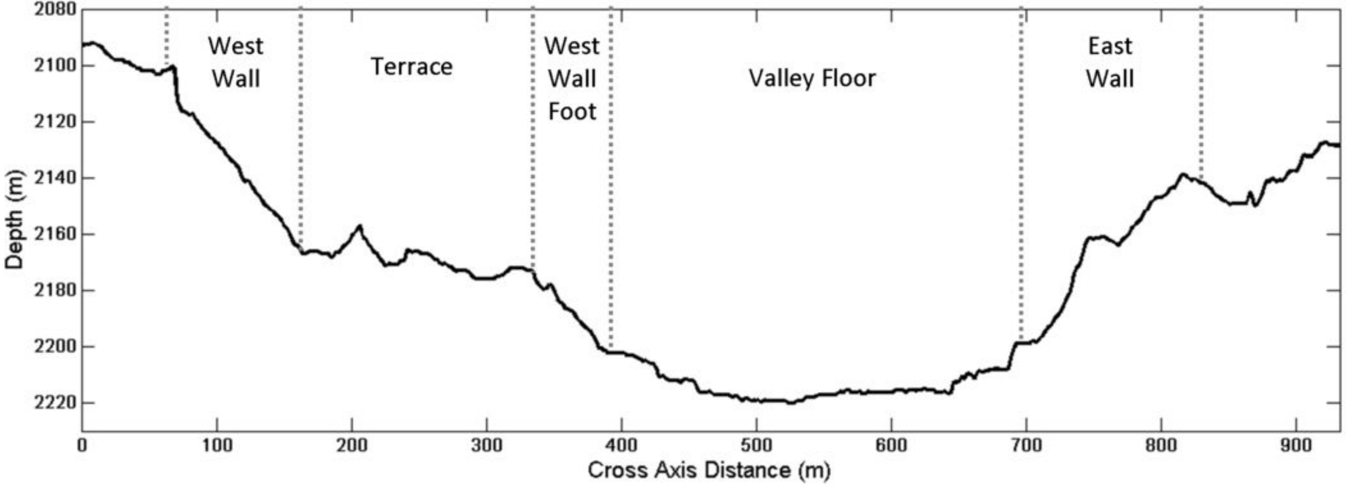

West Wall
Terrace
West Wall Foot
Valley Floor
East Wall
Depth (m)
2080
2100
2120
2140
2160
2180
2200
2220
0
100
200
300
400
500
600
700
800
900
Cross Axis Distance (m)

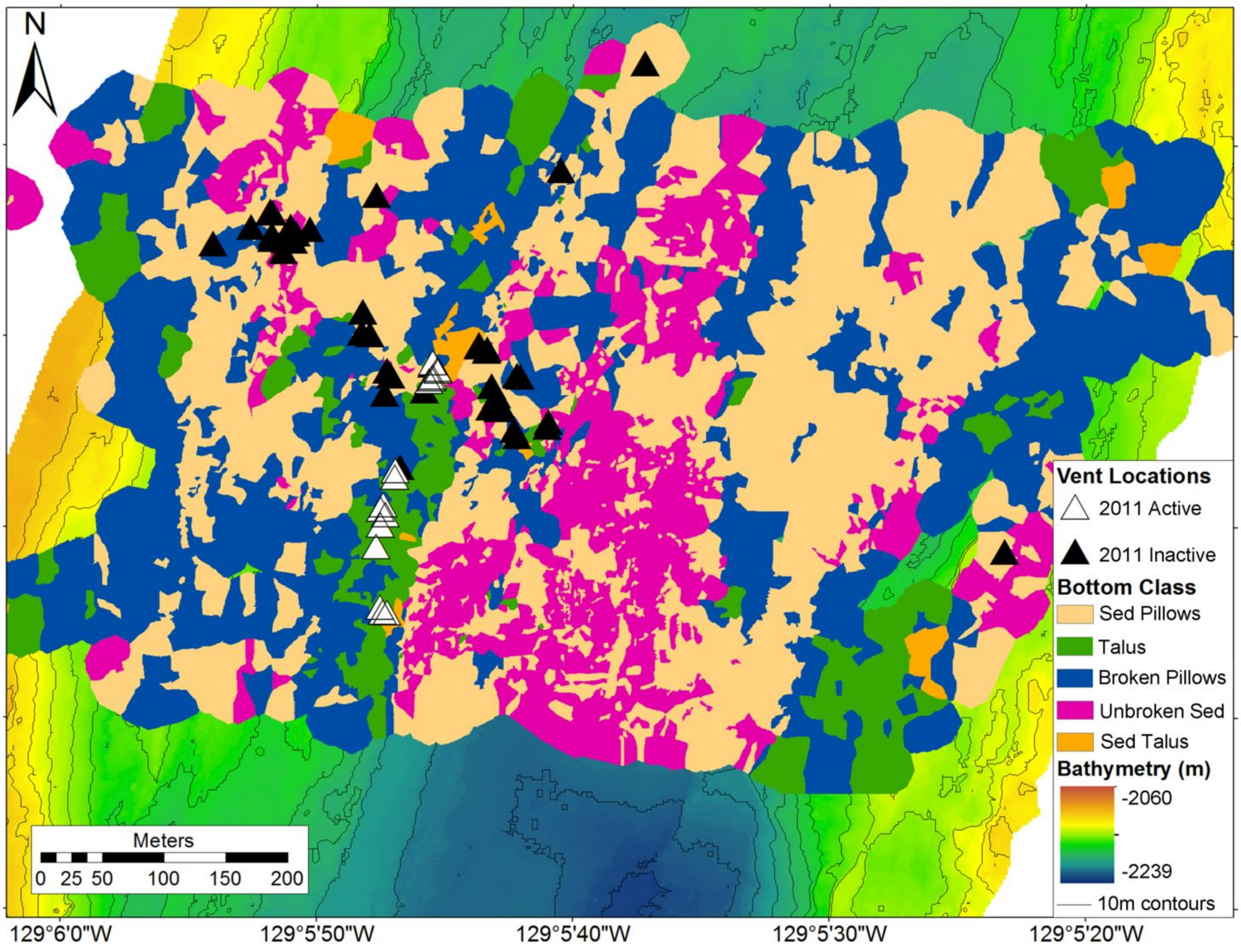
N
47°57'25"N
47°57'20"N
47°57'15"N
47°57'10"N
129°6'0"W
129°5'50"W
129°5'40"W
129°5'30"W
129°5'20"W
Vent Locations
2011 Active
2011 Inactive
Bottom Class
Sed Pillows
Talus
Broken Pillows
Unbroken Sed
Sed Talus
Bathymetry (m)
-2060
-2239
10m contours
Meters
0 25 50 100 150 200

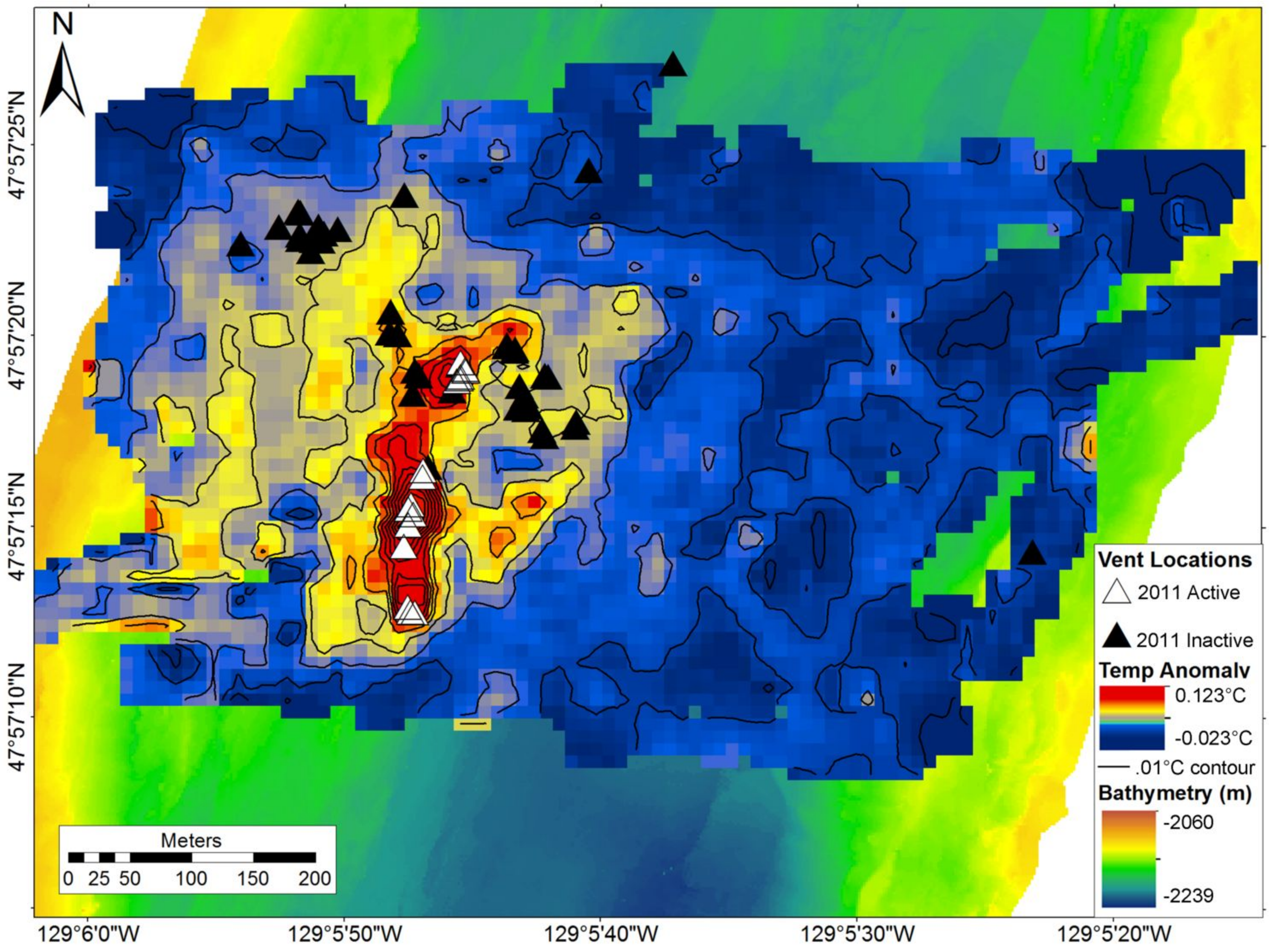
N
47°57'25"N
47°57'20"N
47°57'15"N
47°57'10"N
129°6'0"W
129°5'50"W
129°5'40"W
129°5'30"W
129°5'20"W
Meters
0 25 50 100 150 200
Vent Locations
2011 Active
2011 Inactive
Temp Anomaly
0.123°C
-0.023°C
.01°C contour
Bathymetry (m)
-2060
-2239

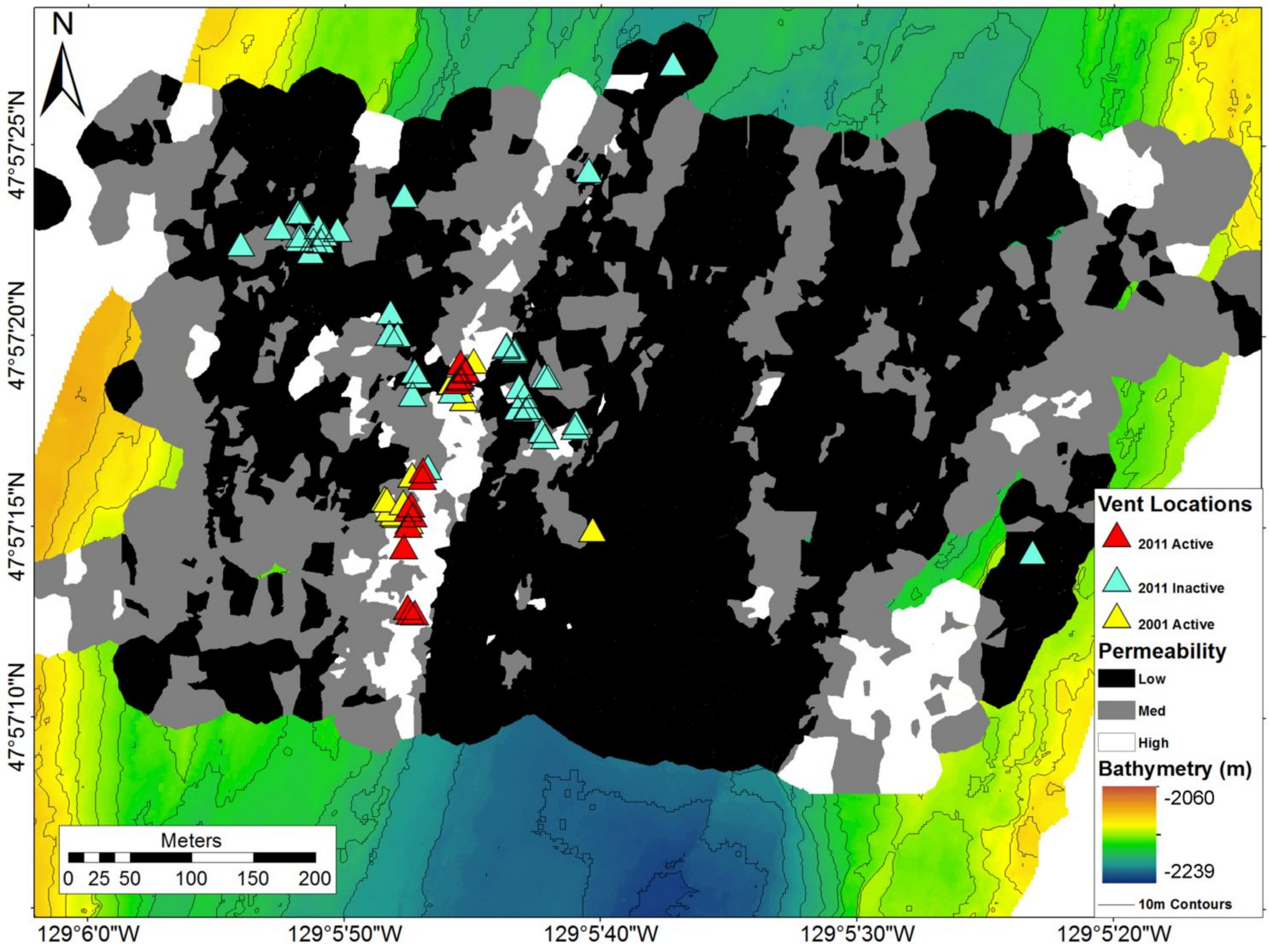

N
47°57'25"N
47°57'20"N
47°57'15"N
47°57'10"N
Vent Locations
2011 Active
2011 Inactive
2001 Active
Permeability
Low
Med
High
Bathymetry (m)
-2060
-2239
10m Contours
Meters
0 25 50 100 150 200
129°6'0"W
129°5'50"W
129°5'40"W
129°5'30"W
129°5'20"W

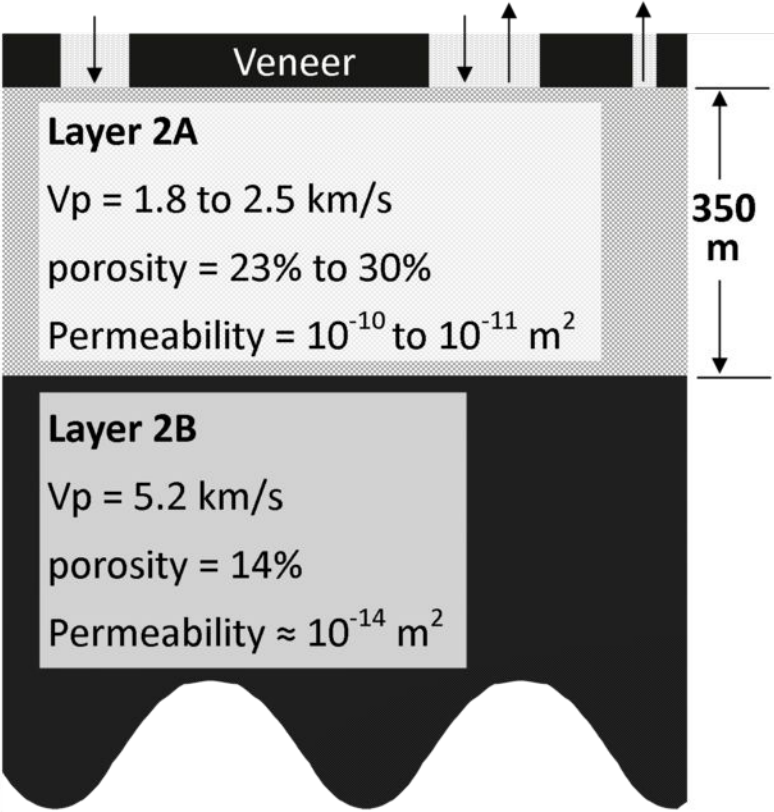

Veneer
Layer 2A
Vp = 1.8 to 2.5 km/s
porosity = 23% to 30%
Permeability = 10^{-10} to 10^{-11} m^2
350 m
Layer 2B
Vp = 5.2 km/s
porosity = 14%
Permeability ≈ 10^{-14} m^2